Spatial mapping of the hepatocellular carcinoma landscape identifies unique intratumoural perivascular-immune neighbourhoods

Felix Marsh-Wakefield[†1,2], Cositha Santhakumar[†1,2,3], Angela L. Ferguson[†1,2], Thomas M. Ashhurst[4,5], Joo-Shik Shin[6,7], Fiona H. X. Guan[3], Nicholas J. Shields[4], Barry J. Platt[2], Ruta Gupta[6,7], Michael Crawford[8], Carlo Pulitano[8,9], Charbel Sandroussi[8,9], Jerome M. Laurence[8,9], Ken Liu[1,3,4], Geoffrey W. McCaughan[‡1,3,4], Umaimainthan Palendira[‡2]

[†/‡]Authors contributed equally

[1]Liver Injury & Cancer Program, Centenary Institute

[2]Human Immunology Laboratory, School of Medical Sciences, Faculty of Medicine and Health, The University of Sydney

[3]A.W. Morrow Gastroenterology and Liver Centre, Royal Prince Alfred Hospital

[4]School of Medical Sciences, Faculty of Medicine and Health, The University of Sydney

[5]Sydney Cytometry Core Research Facility, The University of Sydney

[6]Central Clinical School, Sydney Medical School, The University of Sydney

[7]Department of Tissue Pathology and Diagnostic Oncology, Royal Prince Alfred Hospital, NSW Health Pathology

[8]Australian National Liver Transplant Unit, Royal Prince Alfred Hospital

[9]Royal Prince Alfred Institute of Academic Surgery, University of Sydney

Author contributions

Felix Marsh-Wakefield, Cositha Santhakumar, and Angela L. Ferguson contributed substantially to the conception and design of the paper; acquisition of data; analysis and interpretation of data; drafting and revising the paper extensively and critically for important intellectual content. Thomas M. Ashhurst contributed substantially to the analysis and interpretation of data; revising the paper critically for important intellectual content. Joo-Shik Shin, Fiona H. X. Guan, Nicholas J. Shields, Barry J. Platt, Ruta Gupta, Michael Crawford, Carlo Pulitano, Charbel Sandroussi, and Jerome M. Laurence contributed substantially to acquisition of data; revising the paper critically for important intellectual content. Ken Liu

contributed substantially to the conception and design of the paper; interpretation of data; revising the paper extensively and critically for important intellectual content. Geoffrey W. McCaughan and Umaimainthan Palendira contributed substantially to the conception and design of the paper; interpretation of data; drafting and revising the paper extensively and critically for important intellectual content. All authors provided final approval of the version to be published.

Address of correspondence

Felix Marsh-Wakefield

f.marsh-wakefield@centenary.org.au

Centenary Institute, Camperdown 2050, NSW, Australia

Financial support and sponsorship

This work was funded by the Joan Krefft bequest to the A.W. Morrow Gastroenterology and Liver Centre (Royal Prince Alfred Hospital) and Cancer Institute NSW (2021/ATRG2028). Felix Marsh-Wakefield is supported by the International Society for the Advancement of Cytometry (ISAC) Marylou Ingram Scholars Program. Cositha Santhakumar is supported by the Sydney Cancer Partners PhD scholarship.

Conflicts of interest

Nothing to report.

Keywords

Tumour immunology

Spatial proteomics

Imaging mass cytometry

Human liver cancer

56 Perivascular macrophages

57

58 **List of abbreviations**

59 HCC	Hepatocellular carcinoma
60 VEGF	Vascular endothelial growth factor
61 TME	Tumour immune microenvironment
62 IMC	Imaging mass cytometry
63 FFPE	Formalin-fixed paraffin embedded
64 MVI	Microvascular invasion
65 H&E	Haematoxylin and eosin
66 ROI	Region of interest
67 TIL	Tumour-infiltrating lymphocyte
68 TMA	Tissue microarray
69 IHC	Immunohistochemistry
70 RT	Room temperature
71 mIHC	Multiplex immunohistochemistry
72 TSA	Tyramide signalling amplification
73 PCA	Principal component analysis
74 sPLS-DA	Sparse partial least squares-discriminant analysis
75 TNM	Tumour-node-metastasis
76 PERMANOVA	Permutational multivariate analysis of variance
77 PVM	perivascular macrophage
78 TGF-β	transforming growth factor-beta
79 TAM	tumour-associated macrophage

MRS	myeloid response score
MAIT cells	mucosal-associated invariant T cells

Abstract

Background & Aims: Hepatocellular carcinoma (HCC) develops in the context of chronic inflammation, however, the opposing roles the immune system plays in both the development and control of tumours is not fully understood. Mapping immune cell interactions across the distinct tissue regions could provide greater insight into the role individual immune populations have within tumours.

Approach & Results: Using highly multiplexed imaging mass cytometry, we have mapped the immune landscape of tumour, invasive margin, and adjacent non-tumour regions across sixteen resected tumours comprising of 144 regions of interest and over 10,000 parameters. We show immune cell densities remain largely consistent across these three regions, except for subsets of monocyte-derived macrophages which are enriched within the tumours. Mapping cellular interactions across these regions in an unbiased manner identifies immune neighbourhoods comprised of tissue-resident T cells, dendritic cells, and various macrophage populations around perivascular spaces. Importantly, we identify multiple immune cells within these neighbourhoods interacting with $VEGF^+$ perivascular macrophages.

Conclusions: Cellular interactions, but not cell densities, differ between intratumoural and adjacent non-tumour regions in HCC. Unique intratumoural immune neighbourhoods around the perivascular space points to an altered landscape within tumours. Enrichment of $VEGF^+$ perivascular macrophages within these tumours could play a key role in angiogenesis and vascular permeability.

Introduction

Liver cancer is the sixth most incident cancer and the third leading cause of cancer-related death in the world [1] with hepatocellular carcinoma (HCC) accounting for approximately 90 % of cases [2]. The five-year overall survival of HCC after diagnosis is approximately 20 % and this statistic has not changed significantly over the past decade despite advancements in treatment options [3]. This poor prognosis is attributable to its phenotypic and genetic heterogeneity, its occurrence in patients with reduced liver reserve (cirrhosis), high rates of tumour recurrence following curative treatments, and its predisposition to metastasise in advanced stages [4]. Although immunotherapy has recently revolutionised the treatment of advanced-stage disease in other malignancies such as melanoma and lung cancer, objective

114 response rates to systemic combination therapies in advanced HCC have been suboptimal (less
115 than 30 %) [5-7].

116

117 Being the prototypical cancer of inflammatory origin, immune responses in HCC are
118 implicated in both pro- and anti-tumoural activities [8]. Understanding the complex interplay
119 between immune cells and the tumour environment is therefore critical. Recent studies using
120 single-cell approaches have identified the diverse phenotype of immune cells within HCC
121 tumours and provided some insight into their possible functional roles [9]. However, several of
122 these single-cell methodologies lack spatial context, therefore limiting our ability to determine
123 the potential impact that specific cellular interactions have on clinical outcomes. Spatially
124 resolving these cellular interactions could provide greater insight into how various immune
125 populations contribute to tumour development, progression, and control.

126

127 Angiogenesis is also a key feature of HCC, wherein hypervascularisation and leaky vessels
128 pose challenges to the cellular immune control of tumours and influences responses to various
129 therapies [10-12]. Amongst many angiogenic factors, vascular endothelial growth factor (VEGF)
130 has been identified as the key driver of neovascularisation in HCC, with tumour cells largely
131 implicated in its production [13,14]. The importance of angiogenesis (and its interplay with the
132 tumour immune microenvironment, TME) is evident by recent data showing that combination
133 bevacizumab (anti-VEGFA) and atezolizumab (anti-PD-L1) antibodies improved survival in
134 patients with advanced unresectable HCC [5]. Interestingly, this strategy has been found to have
135 a synergistic effect [15,16]. However, what role immune cells have in angiogenesis and vascular
136 permeability in HCC remains unclear.

137

138 In this study, we interrogated the tumour and adjacent non-tumour immune microenvironment
139 in patients with resectable HCC using a high-dimensional tissue imaging platform known as
140 imaging mass cytometry (IMC). We spatially resolved cellular interactions in these regions to
141 identify immune neighbourhoods in intratumoural perivascular spaces that comprised of liver-
142 resident $CD4^+$ and $CD8^+$ T cells, dendritic cells, and phenotypically diverse macrophages.
143 Importantly, we showed enrichment of $VEGF^+$ perivascular macrophages within the tumour

144 regions that interact with these immune aggregates in the perivascular space, suggesting these
145 immune neighbourhoods could be important in the development and/or progression of HCC.

146

Methods

Patients

Institutional human research ethics was obtained by the Sydney Local Health District Ethics Review Committee (HREC 2020/ETH02093). Research was conducted in accordance with both the Declarations of Helsinki and Istanbul, with written consent given in writing by all subjects. Treatment naïve patients undergoing curative resection for HCC from 2019 until 2021 at a single tertiary institution were identified from the Royal Prince Alfred Liver Biobank. The formalin-fixed paraffin embedded (FFPE) tissues were retrieved from the Department of Tissue Pathology and Diagnostic Oncology and Royal Prince Alfred Hospital. Relevant clinicopathological data was obtained from electronic medical records. Clinicopathological data included age, sex, aetiology of liver disease, presence of cirrhosis, presence of microvascular invasion (MVI), and largest tumour size. Of the sixteen HCC patients, two have since begun treatment with immune checkpoint inhibitors, and one is now part of a placebo-controlled trial.

Tissue Microarray Preparation

The haematoxylin and eosin (H&E) stained sections from the sixteen patients were reviewed by a liver pathologist. One region of interest (ROI) was selected from the tumour, invasive margin, and peritumour regions. The tumour ROI was selected based on the high abundance of tumour-infiltrating lymphocytes (TILs) on H&E stained sections. The invasive margin was defined at the border of the malignant tumour and consisted of approximately 50 % malignant and 50 % non-malignant tissue. The peri-tumour region was selected away from the tumour. Three 1 mm diameter (triplicate) cores were taken from each ROI for creation of the two tissue microarrays (TMAs) (Figure 1A). Tonsils and hepatocellular adenoma were used as batch controls for the TMAs. Both TMAs were sectioned at 7 µm onto charged slides. Figure 1 provides an overview of the experimental design.

Antibody Panel

An antibody panel (Supplementary Table 1) was designed to identify various components of the HCC TME and background liver tissue, including malignant and non-malignant

177 hepatocytes, immune cells, immune checkpoint inhibitors, cell signalling pathways, stromal
178 cells, and structural markers. Antibodies were selected based on clones previously validated in
179 our lab on FFPE liver tissue and from published studies in HCC [17]. Antibodies that were
180 purchased unconjugated were all tested and validated by conventional immunohistochemistry
181 (IHC) prior to metal conjugation. Post-metal conjugation antibodies were revalidated and
182 titrated using IMC. Pre-conjugated antibodies (Sydney Cytometry Reagent Bank) were tested
183 and titrated for our tissue and staining conditions prior to experimental use. Antibody-metal
184 conjugations were done using the X8 Maxpar conjugation kit as per the manufacturer's
185 protocol (Standard BioTools).

186

187 **Tissue staining for imaging mass cytometry**

188 TMA sections were baked at 60 °C for 60 minutes prior to deparaffinisation and rehydration.
189 Heat-induced antigen retrieval was performed by boiling the samples at 100 °C for 15 minutes
190 in pH 9.0 antigen retrieval buffer (10 mmol L^{-1} Tris base, 1 mmol L^{-1} EDTA, 0.05 % Tween
191 20, pH 9.0). The TMA slides were allowed to cool down to room temperature (RT) before
192 proceeding.

193 Sections were incubated with 3 % hydrogen peroxide prior to washing and blocking (Akoya
194 Biosciences, Antibody Diluent/Block). Slides were then stained with anti-CD69 (clone
195 EPR21814, Abcam) at RT before washing with TBS-T. Secondary OPAL-HRP (PerkinElmer)
196 was added to the slides at RT before washing in TBS-T. Slides were stained with TSA Plus
197 FITC (PerkinElmer) at RT before washing with TBS-T. Slides were microwave treated (as
198 described above) before letting them cool down to RT before proceeding.

199 Slides were then washed in TBS-T before blocking in blocking buffer (Akoya Biosciences) for
200 45 minutes at 37 °C. Slides were blocked with 20 % donkey serum (in DPBS) for 10 minutes
201 at RT. Slides were stained with anti-PD-L1 (clone E1L3N, CST) and anti-CK8/18 (clone 5D3,
202 Leica) for 45 minutes at RT before washing in TBS-T. Slides were then stained with Cy3 anti-
203 rabbit (711-166-152, Jackson ImmunoResearch Laboratories) for PD-L1 and Cy5 anti-mouse
204 (715-606-150, Jackson ImmunoResearch Laboratories) for CK8/18. Slides were washed in
205 TBS-T and DPBS. Slides were avidin/biotin blocked (Life Technologies). Slides were then
206 stained in anti-Foxp3 biotin (clone 236A/E7, eBioscience) before washing in TBS-T. TMA
207 sections were incubated overnight with a metal-tagged antibody cocktail (Supplementary Table
208 1, including anti-FITC, anti-Cy3, anti-Cy5, and anti-biotin) at 4 °C.

209 TMA sections were washed in 0.1 % Triton-X (in DPBS) and DPBS. TMA sections were
210 stained with Cell-ID Ir-Intercalator in DPBS (Standard BioTools). TMA sections were washed
211 in deionised H_2O before being allowed to air dry at RT (Figure 1B).

212

213 **Imaging Mass Cytometry**

214 The Hyperion imaging mass cytometer (Standard BioTools) was used to acquire data from
215 both TMA slides. A pulsed laser scanned and laser ablated the tissue at 200 Hz. IMC data files
216 were analysed using MCD Viewer (version 1.0.560.6, Standard BioTools). MCD Viewer and
217 histoCAT++ [18] were used for visualising the images, TIFF extraction, and creating
218 representative pseudo-colour images. (Figure 1C-D).

219

220 **Multiplex Immunohistochemistry**

221 FFPE tumour specimen blocks were sectioned at 4 µm and stained using OPAL multiplex IHC
222 (mIHC) staining kit (Akoya Biosciences) according to optimised in-house protocols as
223 previously described [19,20]. Tissue sections were baked at 60 °C for 60 minutes prior to
224 deparaffinisation and rehydration. Heat-induced antigen retrieval was performed by boiling the
225 samples at 100 °C for 15 minutes in pH 9.0 antigen retrieval buffer. Sections were incubated
226 with 3 % hydrogen peroxide prior to washing and blocking (Antibody Diluent/Block, Akoya
227 Biosciences). Sections were then incubated with a single purified primary antibody for 35
228 minutes at RT, washed, and then incubated with HRP (OPAL polymer HRP (Akoya
229 biosciences), sheep-HRP (Invitrogen), or MACH-3 mouse 2-step (Biocare, 10 minutes/step))
230 for 10 minutes at RT. Sections were washed prior to incubation with OPAL fluorochromes
231 diluted in tyramide signalling amplification (TSA) reagent (Akoya Biosciences). Antigen
232 retrieval was repeated, and subsequent antibodies stained for as described above. At completion
233 of all antibody staining, samples were counterstained for DAPI (Cell Signalling Technologies)
234 prior to mounting with Prolong Diamond (Life Technologies).

235 Primary antibodies used were anti-HLA-DR (TAL-1B5, Abcam), anti-FXIIIa (SAF13A,
236 Affinity Biologicals), anti-CD34 (QBEnd/10, Leica), and anti-VEGF (VG1, Dako).

237 Representative high-powered images (20X and 40X) within tumour regions were captured
238 using the Mantra quantitative pathology imaging system in combination with Mantra snap

239 (Akoya Biosciences) and inForm (Akoya Biosciences) to spectrally process images.
240 Multispectral images were exported as TIFF single images and were imported into Fiji (version
241 1.53c) [21].

242

243 **Spatial data Analysis**

244 Ilastik software (version 1.4.0b27) was used to segment single cells using the multicut method
245 [22], as this method does not rely on nuclei (Figure 1C). Masks were created to then quantify
246 marker expression levels for each single cell in R [23] using 'Spectre' [24] (Figure 1D).

247 Single cells were manually gated using FlowJo (version 10.8, BD Bioscience) to identify
248 conventional immune cell subsets (Supplementary Figure 1). The area of each section was
249 calculated using Fiji (version 1.53c) [21], which was then used to calculate the density of each
250 conventional subset. Spectre was then used to quantify, for every cell, the average number of
251 each cell subset within a 20 µm radius.

252 For unsupervised analysis, X-shift clustering was used [25], which identified 238 clusters
253 (Supplementary Figure 2A). The median signal intensity of CD45 was calculated for each
254 cluster before running z-score normalisation. Clusters with values below zero were considered
255 $CD45^{-}$, and values above zero were considered $CD45^{+}$. The latter were divided into $CD45^{low}$
256 and $CD45^{hi}$ with a cut-off equal to the absolute value of the smallest value (Supplementary
257 Figure 2B). Cells then underwent X-shift clustering within each of the three groups ($CD45^{-}$,
258 $CD45^{low}$, and $CD45^{hi}$) resulting in 91, 36, and 18 clusters respectively. Similar clusters were
259 then combined using the function simprof as part of the 'clustsig' R package [26], generating 47
260 clusters (20 $CD45^{+}$ clusters and 27 $CD45^{-}$ clusters) (Supplementary Figure 2C). The spatial
261 data were then quantified using Spectre [24], including cluster densities, average distance
262 between each cluster and every other cluster, average number of cells within 20 µm for each
263 cluster, and the proportions of each cluster. As each region was done in triplicate, the results
264 were averaged so each patient tissue region had a single value for each quantification.

265 When analysing the $CD45^{+}$ clusters, the number of clusters with ≥ 5 cells in each region were
266 calculated. Clusters with < 5 cells across less than a third of total regions were excluded, which
267 removed six clusters (Supplementary Figure 2D).

268 Heatmaps were generated using Spectre. The median signal intensity for each cluster was
269 calculated and then min-max scaled.

Each patient region contained thousands of parameters, so linear dimensionality reduction algorithms were used to reduce the complexity. A principal component analysis (PCA) was performed using Spectre to identify differences between the three tissue ROIs: non-tumour, invasive margin, and tumour. A PCA reduced the dimensions based on the overall variance within a given dataset, including human and experimental variability. In addition to a PCA, a sparse partial least squares-discriminant analysis (sPLS-DA) was done [27]. An sPLS-DA reduces the dimensions based on differences between groups and is not as strongly affected by unwanted variability. The R package 'mixOmics' was used for the sPLS-DA [28]. The sPLS-DA used leave-one-out validation, calculating the Mahalanobis distance with at least three components generated. When using all clusters, up to ten variables were selected for each component. For select immune cell neighbourhood interactions, there was no limit to the number of variables assessed for each component.

Ligand-receptor communication

Single-cell transcriptomic analyses were done using the GSE149614 dataset, which consisted of cells from paired non-tumour and tumour (8/10 patients) from newly diagnosed HCC patients [29]. These patients were pathologically confirmed and proven to have no other cancers. 7/10 patients had viral infection (five with HBV, two with HCV), 3/10 had tumour-node-metastasis (TNM) stage I, 1/10 had stage II, 2/10 stage IIIA, 2/10 stage IIIB, and 2/10 stage IV [29]. Pre-processed and pre-annotated data were used. Ligand-receptor communication between cells was calculated using the R package 'CellCall' [30].

Statistical tests

Statistics were calculated using packages available within R [23], using Type III Sum of Squares, unless stated otherwise. Plots were generated using R and GraphPad Prism (version 9.0.0). For the PCA, a permutational multivariate analysis of variance (PERMANOVA) was done. The data were scaled with the Euclidean distance calculated between datapoints. Permutational tests are powerful non-parametric tests that do not assume homogeneity of variance or normality of distribution [31]. 4,999 permutations (for a total of 5,000 tests) were done using all parameters to compare between groups (non-tumour, invasive margin, and tumour regions). The R package 'vegan' was used for PERMANOVA calculations [32]. To calculate paired p-values between

301 groups, the R package 'pairwiseAdonis' was used with Holm's correction for multiple
302 comparisons [33]. A similar method was used for the sPLS-DA, but only the parameters that were
303 identified in the first two components were used in their calculation.

304 For the manually gated results, a Friedman test with Dunn's multiple comparison corrections
305 was done to compared between groups (non-tumour, invasive margin, and tumour regions).
306 For comparisons between non-tumour and tumour, a Wilcoxon test was used. These were
307 calculated in Graphpad Prism (version 9.0.0).

308 For comparisons between non-tumour and tumour, a PERMANOVA with Holm's correction
309 was used for the sPLS-DA (as above). For paired comparisons for individual parameters a
310 permutation student's t-test was done using the perm.t.test function as part of the
311 'RVAideMemoire' R package [34].

312

313 **Results**

314 **Study design**

315 Sixteen treatment naïve HCC patients who underwent liver resections were included in this
316 study. Of these patients, twelve were male and the median age was 64.5 years (range 33-84
317 years). The aetiology of chronic liver disease was viral in seven patients, non-viral in eight
318 patients, and dual viral and non-viral pathology in one patient. Nine patients were cirrhotic,
319 and half the cases had evidence of microvascular invasion. The median largest tumour size was
320 36 mm (range 9-270 mm). Quantitative protein expression on single cells and spatial mapping
321 of cellular neighbourhood interactions were performed on patient tissue samples from selected
322 regions (non-tumour, invasive margin, and tumour) (Figure 1C-D).

323

324 **The spatial landscape differs between HCC tumour regions**

325 We mapped the full cellular landscape (immune cells, stromal cells, endothelial cells,
326 hepatocytes, and tumour cells) of HCC to identify any differences between non-tumour,
327 invasive margin, and tumour regions. X-shift clustering was initially performed on all cells.
328 This unbiased approach identified 47 clusters (Figure 2A). The spatial environment was
329 quantified for each patient and tissue region. A PCA was run on > 10,000 parameters, including
330 individual cluster levels (density, percentage of total cells, count), average distances between
331 clusters, and neighbour interactions across each region. Neighbourhood interactions were
332 inferred based on the average number of one cluster within 20 µm of another (or same) cluster
333 [35]. The PERMANOVA revealed significant differences between the three regions (p=0.0030),
334 which was limited to a difference between non-tumour and tumour (p=0.0006) but not between
335 invasive margin and tumour or non-tumour (Figure 2B, p=0.2467). We then determined the
336 parameters that contribute most to the identified variance. This revealed the primary
337 differentiator as the distance between individual clusters, suggesting that the spatial distribution
338 of cells could be key in HCC (Figure 2C). Using a more targeted approach that provides greater
339 granularity to the parameters that potentially differentiate these regions, the sPLS-DA also
340 showed clear differences between each of the three regions (Figure 2D). The differentiating
341 parameters included not only distance between clusters, but also cell proportions and densities
342 (Figure 2E). Component 1 (represented by the x-axis) separated all regions. Cluster 37,
343 identified as endothelial cells, had differences in density, percentage, and count. Cluster 34,
344 another endothelial cell subset, differed in percentage and count. Neighbourhood interactions

345 of cluster 44 (myeloid cells) to 16 (hepatocytes), cluster 12 (hepatocytes) to 34 (endothelial
346 cells), and cluster 12 (hepatocytes) to 37 (endothelial cells) also differed between regions,
347 particularly between non-tumour and tumour regions. Component 2 (y-axis) separated the
348 invasive margin, with neighbourhood interactions of cluster 3 (T cells) to 28 (endothelial cells).
349 Together, these data show that our unbiased analytical approach to identify differences in HCC
350 tissue regions demonstrates clear distinctions in the overall cellular landscape. We were
351 particularly interested in the immune cell microenvironment within these regions. Thus, we
352 specifically examined quantities and spatial relationships of immune cells.

353

354 **Innate, but not adaptive, immune cell densities differ between HCC and adjacent tissue**

355 Differences in the immune landscape of the tumour, invasive margin, and adjacent non-tumour
356 regions were investigated to determine whether cell densities differentiated the three regions.
357 Manual gating analysis was performed to identify conventional immune cell subsets, including
358 both innate and adaptive immune populations (Figure 3). Surprisingly, the densities of these
359 immune subsets were mostly similar across the three regions. T cells (particularly $CD4^+$ T
360 cells) constituted the largest proportion of immune cells across all regions and their densities
361 remained consistent (Figure 3A-B, Supplementary Figure 3A). Of the myeloid cells,
362 macrophages constituted the largest proportion across regions (Figure 3A). There was a higher
363 density of macrophages and dendritic cells within tumour compared to non-tumour regions
364 (Figure 3B).

365 A more targeted analysis of innate immune cell subsets revealed subsets of macrophages
366 ($CD16^+$ $CD68^+$ $CD206^+$ $CD11c^{+/-}$), possibly monocyte-derived (based on CD14 expression),
367 were significantly higher within tumour compared with non-tumour regions (Figure 3C). In
368 contrast, $CD11c^+$ and $CD11c^-$ macrophages that were $CD14^-$ were not different
369 (Supplementary Figure 3B). These subsets were also higher (as a proportion of total cells) in
370 the tumour compared with non-tumour regions, with the exception of monocyte-derived
371 $CD206^+$ $CD11c^-$ macrophages (Supplementary Figure 3C). As a proportion of total immune
372 cells, only the monocyte-derived $CD11c^+$ macrophages were higher in the tumour compared
373 with non-tumour regions (Supplementary Figure 3C).

374 There were no significant differences in the density of T cell subsets between regions (Figure
375 3B). Most T cells were $CD4^+$ rather than $CD8^+$ across regions, with most $CD4^+$ T cells
376 expressing CD69, consistent with tissue-resident $CD4^+$ T cells (Supplementary Figure 3A).

377 Together, these data demonstrate that innate immune cells, particularly monocyte-derived
378 macrophages, are significantly increased within tumour when compared to non-tumour
379 regions.

380

381 **Unique immune cell neighbourhood interactions exist within the HCC tumour**

382 As the densities and proportions of most conventional immune cell subsets were similar across
383 regions, we next spatially analysed these regions to investigate immune cell neighbourhood
384 interactions. When investigating $CD45^+$ clusters alone to focus on immune cells, six clusters
385 had < 5 cells in more than one third of the images, so were removed from further analysis
386 (Supplementary Figure 2D). Furthermore, certain clusters were phenotypically similar to each
387 other and were combined (Supplementary Figure 4). As a result, ten $CD45^+$ clusters were
388 included in the neighbourhood analysis (Figure 4A).

389 To identify immune cell interactions that differ between regions, an sPLS-DA was performed
390 that revealed differences in immune cell neighbourhood interactions between non-tumour and
391 tumour regions (Figure 4B). Multiple immune cell neighbourhood interactions were identified
392 (Figure 4C). The first component (x-axis) parameters were further investigated. Cluster 44 was
393 more commonly within 20 µm of other clusters (including 3, 8, 9, 35, 44) within tumour
394 compared to non-tumour regions. Likewise, cluster 35 was commonly within 20 µm of cluster
395 45, and cluster 9 within 20 µm of cluster 8 within HCC tumour regions. These seven immune
396 cell neighbourhood interactions were identified to be more common within tumour regions
397 when compared to non-tumour regions (Figure 4D). We then determined whether these
398 interactions could have been impacted by individual cell densities. The density of clusters 8, 9,
399 44, and 45 was higher within tumour compared to non-tumour whilst the opposite was true for
400 cluster 35 (Figure 4E). There was no difference in the density of cluster 3 when comparing
401 tumour and non-tumour regions. These data show that multiple immune cell neighbourhood
402 interactions are more frequent within HCC tumour regions when compared to non-tumour
403 regions. Some of these increased neighbourhood interactions may be attributed to increased
404 densities of the cells involved.

405

406 **Increased immune cell interactions with $VEGF^+$ perivascular macrophages in HCC**
407 **tumour tissue**

408 Having identified cluster 44 at the centre of multiple neighbourhood interactions, this cell
409 cluster was investigated further. Closer examination of the expression markers associated with
410 cluster 44 revealed expression of both CD45 (indicating a haematopoietic cell) and tumour
411 endothelial marker CD34 (Figure 5A). This prompted us to closely examine all images to
412 determine potential close interactions between two different cell types (Supplementary Figure
413 5). We found that cluster 44 was in fact two discrete cells in close proximity: a tumour
414 endothelial cell characterised by CD34 expression, and a myeloid cell which on further
415 phenotyping also expressed CD14, CD16, CD45, CD68, CD86, CD206, FXIIIA, and HLA-
416 DR, but not CD11c (Figure 5B). Based on the close proximity of this myeloid cell to the tumour
417 endothelial cell with reference to the phenotypic markers expressed, we hypothesised the
418 myeloid cell to be a perivascular macrophage (PVM). Further staining using mIHC, which
419 allowed for greater image resolution, showed that this PVM-like cell also expressed VEGF,
420 suggesting they are indeed PVMs (Figure 5C) [36-38].

421

422 To determine whether any cell-cell communication was occurring between the $CD34^+$
423 endothelial cells and the $VEGF^+$ PVM, publicly-available single-cell transcriptomic data were
424 analysed. The GSE149614 dataset consisted of tumour resections from newly diagnosed HCC
425 patients with paired non-tumour and tumour tissue cell dissociates [29]. The pre-annotated data
426 included endothelial cells expressing *Cd34* (C48) and macrophages expressing *Vegfa* (C21)
427 that we considered to most closely resemble PVM. Ligand-receptor communication was
428 inferred using 'CellCall' [30]. When C48 (*Cd34*$^+$ endothelial cells) acted as the ligand, several
429 chemokine ligands were predicted to interact with chemokine receptors on C21 in both non-
430 tumour and tumour regions (Figure 5D). When C21 (*Vegfa*$^+$ macrophages) acted as the ligand,
431 there was communication within the tumour but not non-tumour tissue with endothelial cell
432 (C48) receptors. Furthermore, *Vegfa* and *Tgfb1* were predicted ligands from C21, suggesting
433 the $VEGF^+$ macrophages are communicating with $CD34^+$ endothelial cells. Together these data
434 reveal that tumour regions are not only highly enriched with $CD34^+$ tumour endothelial cells,
435 but also have $VEGF^+$ PVM that potentially interact with these endothelial cells in that region.

436

437 **Perivascular immune cell aggregates consist of liver-resident $CD4^+$ and $CD8^+$ T cells,**
438 **dendritic cells, and macrophages within HCC tumour tissue**

439 Having identified multiple clusters neighbouring with cluster 44, we then defined all clusters
440 that were found in close proximity of cluster 44. Clusters 3 (Figure 6A) and 9 (Figure 6B) were
441 T cells ($CD45^+$ $CD3^+$). Further phenotyping showed cluster 3 to be $CD4^+$ $CD45RO^+$ $CD69^+$,
442 suggestive of liver-resident memory $CD4^+$ T cells, and cluster 9 to be $CD8A^+$ $CD45RO^+$ $CD69^+$
443 $Tbet^+$ PD-$L1^+$, likely liver-resident memory $CD8^+$ T cells (Figure 6C). Both clusters had a
444 higher interaction with cluster 44 within the tumour, suggesting an interaction between $CD4^+$
445 and $CD8^+$ T cells with PVMs and tumour endothelium.

446 Clusters 8 (Figure 6D) and 35 (Figure 6E) were $CD45^+$ $CD14^+$ HLA-DR^+ myeloid cells.
447 Cluster 8 was also $CD11c^+$ $CD16^+$ $CD68^+$ $CD206^+$ $FXIIIA^+$, suggestive of a potential
448 macrophage, while cluster 35 was $CD11c^-$ $CD16^+$ $CD68^+$ $CD206^+$ $FXIIIA^-$, possibly
449 representing a dendritic cell population (Figure 6F). The increased neighbourhood interaction
450 of these cells with PVM-endothelial cell cluster (cluster 44) in the HCC tumour tissue points
451 to an interaction between the tumour endothelium/PVM niche and other myeloid cells within
452 the TME.

453 Cluster 8, a macrophage subset, was also found to have a neighbourhood interaction with
454 cluster 9, a memory $CD8^+$ T cell subset (Figure 7A, Supplementary Figure 6). Clusters 35 (a
455 dendritic cell subset) and 45 were both $CD45^+$ $CD14^+$ HLA-DR^+. Cluster 45 had a macrophage
456 phenotype as $CD16^+$ $CD68^+$ $FXIIIA^+$ (Figure 7C). The neighbourhood interactions between
457 these two myeloid cell populations were also higher in the tumour compared to non-tumour
458 regions (Figure 7B) despite the density of cluster 35 being lower in the tumour compared to
459 the non-tumour regions (Figure 4E). Together, these single cell maps reveal that unique
460 intratumoural immune aggregates (consisting of T cells, dendritic cells, and macrophages)
461 interact with PVM and may exert potential pro-tumoural and angiogenic functions. These
462 findings are summarised in Figure 8.

463

464 Clinical associations were assessed by correlating tumour neighbourhood interactions with
465 prognostic and clinicopathological data. There were no associations between tumour
466 neighbourhood interactions and cirrhosis, early recurrence (<2 years), MVI, or viral-associated
467 HCC (Supplementary Figure 7).

468

469

Discussion

The treatment of HCC remains a major challenge and novel therapeutic strategies are urgently required. Irrespective of its aetiology, HCC mostly develops in diseased liver with concomitant chronic inflammation, thus implicating the immune system in both the pathogenesis of the disease as well as tumour control. Understanding the complex interactions between immune cells and the TME is therefore paramount [39,40]. We used high-dimensional spatial analysis to map multiple cellular neighbourhood interactions across three regions: the non-tumour, invasive margin, and tumour regions. Mapping the immune landscape across these regions showed that only innate cell densities, but not T cell or B cell densities, are increased within tumour regions compared to non-tumour regions and that macrophages (likely monocyte-derived) are enriched within tumour tissue. We further identified immune aggregates around the perivascular space that are unique to the tumour region. Detailed analysis of this region shows that PVMs are at the centre of these interactions and are closely associated with not only the tumour endothelial cells, but also multiple immune populations, including liver-resident $CD4^+$ and $CD8^+$ T cells, macrophages, and dendritic cells. Functionally, we show that these PVMs are capable of producing VEGF, which is known to be a key driver of angiogenesis and hypervascularity within tumours. Mining publicly available single-cell datasets to interrogate potential ligand-receptor interactions between PVMs and endothelial cells confirms VEGF-VEGF receptor interactions and also suggests that other potential pro-tumoural mechanisms involving transforming growth factor-beta (TGF-β) are active within these unique immune aggregates.

How the tumour immune microenvironment and its composition is impacted by hepatocarcinogenesis remains unclear. Our data show enrichment of phenotypically diverse populations of macrophages within the tumour compared to non-tumour regions. Based on CD14 expression, these populations were most likely monocyte-derived [41,42]. This is in-line with the consensus in the field that tumour-associated macrophages (TAMs) are derived primarily from circulating blood monocytes [43], and in human HCC, TAMs arise from $CCR2^+$ monocytes [44]. Interestingly, we found other $CD14^-$ macrophage populations were either reduced within tumours or did not show any difference compared to adjacent non-tumour tissue. This, together with no changes in T cell densities between tumour and non-tumour regions, suggests that the tumour immune microenvironment is largely skewed by the

502 recruitment of monocytes. Furthermore, our findings on several myeloid cell populations
503 regarding their overall numbers and cell-cell interactions should be compared with the findings
504 of Wu *et al.* who devised a myeloid response score (MRS) in using 244 resected human HCC
505 samples [45]. Tumours with a high MRS score were enriched in $CD11b^+$, $CD15^+$, $CD163^+$,
506 $CD33^+$, $CD68^+$, and $CD204^+$ cells. These were thought to be immunosuppressive in nature and
507 associated with poor prognosis. In addition, Kurebayashi *et al.* found that macrophages were
508 the most common immune cell detected in 919 regions from 158 resected HCC tumours [46].
509 CD68 is commonly used as a liver TAM marker [47] and this subset was found to be increased
510 in our tumours. Similarly, $CD206^+$ $CD14^+$ monocyte-derived macrophages were also enriched
511 within the tumour in our study. A dysregulated balance towards $CD206^+$ M2 polarised
512 macrophages has also been associated with aggressive tumour phenotypes and worse prognosis
513 in HCC [48].

514

515 Where these macrophages localise within tumour tissue is critical to our understanding of how
516 the immune environment impacts tumour development, persistence, as well as tumour control.
517 Many previous studies have interrogated the TME in HCC using various techniques including
518 mIHC [45,46,49], IMC [50,51], and multimodal genomic analysis incorporating single-cell RNA
519 sequencing and TCR receptor sequencing [52-54]. However, not all these techniques facilitate
520 spatial analyses to identify cell-cell interactions between multiple different types of cells within
521 the TME. Our study provides a comprehensive analysis of the composition of the tumour
522 immune microenvironment of HCC and adjacent non-tumour tissue whilst further identifying
523 novel cell-cell interactions between immune cells and the tumour vasculature. Through this
524 spatial mapping we have identified a cellular neighbourhood around the endothelium and
525 PVMs of potential importance.

526

527 The close physical association between tumour endothelial cells and macrophages prompted
528 us to define them as PVMs. Currently, there is no consensus on the definition of PVMs as they
529 can have different phenotypes across tissues. However, a unifying feature is that they lie in
530 close proximity to blood vessels, either in direct contact or located within one cell thickness
531 from it [38]. However, PVMs have not yet been described in healthy adult liver tissue. In diseased
532 tissues such as cancer, these cells have been shown to express VEGF [37,38]. We also show that
533 these PVMs are indeed able to produce VEGF. Importantly, pre-clinical models show that

534 PVMs are also largely derived from circulating monocytes [37]. In line with this, Matasubra *et*
535 *al.* found that the majority of angiopoietin ($TIE2^+$) expressing macrophages in liver cancer
536 were located in the perivascular areas of tumour tissue and their presence not only correlated
537 with the degree of angiogenesis, but also with the levels of their counterparts in blood [55].
538 Several other functions of PVMs have been described both in other healthy adult tissues
539 (phagocytosis, antigen presentation, and immune regulation), and in the progression of
540 pathological conditions (angiogenesis, metastasis, immunosuppression, recruitment of other
541 leukocytes, and post-therapy relapse) [38]. It is tempting to postulate that PVMs are critical not
542 only for angiogenesis and hypervascularity in HCC through the secretion of VEGF but are also
543 responsible for the 'leaky' vessels seen in HCC that compromise immune control mechanisms.
544 There is evidence from pre-clinical models to support both these possibilities. TIE2-expressing
545 monocytes were found to be critical for tumour angiogenesis [56], supporting the fact monocyte-
546 derived cells within tumours are key for angiogenesis. In addition, in a murine model of breast
547 cancer, macrophage-specific depletion of VEGFA reduced both vascular permeability and
548 circulating tumour cells whilst restoring vascular junctions [36].

549

550 Our TMA selection criteria of highly abundant TILs on H&E suggest we have selected areas
551 that share features of the *Inflamed Class* of HCC [54]. This class represents approximately 35 %
552 of HCC tumours and is characterised by a microenvironment with increased interferon
553 signalling and higher immune infiltration (increased TILs, macrophages, tertiary lymphoid
554 structures, and elevated expression of checkpoint molecules) compared with non-inflamed
555 tumours [54]. The inflamed subclass exhibits a significantly higher fraction of $CD8^+$ T cells and
556 M1 macrophages when compared to the non-inflamed profiles. However, despite the presence
557 of high TILs, these tumours persist. There could be many factors that contribute to this tumour
558 persistence, including enrichment of clonally exhausted $CD8^+$ T cells and regulatory T cells
559 within HCC tissues [52]. Our finding of no difference in the T cell density between tumour and
560 non-tumour tissues is of interest. We also found that $CD4^+$ T cells were more abundant than
561 $CD8^+$ T cells within the HCC TME, consistent with previous studies [46]. Furthermore, $CD4^+$ T
562 cells expressing CD69 were the most common subset of $CD4^+$ T cells across all regions in our
563 study. Importantly, we found close interactions between these T cells and PVMs in the
564 perivascular space. This niche could facilitate regulatory interactions for effector and resident
565 T cells. We also identified multiple myeloid cells interacting with T cells within this niche,

566 although the functional role of these myeloid cells remains unknown. Further studies are
567 required to identify how and why T cells are potentially impaired within such tumour regions.

568

569 The findings from our study have several clinical implications. The identification of increased
570 TIL density within a perivascular-immune neighbourhood (consisting of tumour endothelial
571 cells and PVMs) warrants discussion of current therapeutic approaches that target immune-
572 vascular cross-talk and the role of vascular normalisation in HCC [57]. The tumour vasculature
573 in HCC is structurally and functionally abnormal, and the tumour vessels are excessively leaky
574 [58]. Immune-vascular cross-talk underpins the rationale for using bevacizumab, an anti-VEGFA
575 monoclonal antibody that normalises tumour vasculature, in conjunction with immune
576 checkpoint inhibitors in advanced unresectable HCC [5]. Advanced colorectal cancer patients
577 receiving combined FOLFOX and bevacizumab have decreased VEGFB-mediated
578 angiogenesis, including reduced myeloid cell-endothelial cell communication via VEGF as
579 identified by single-cell RNA sequencing [59]. In pre-clinical HCC models, anti-angiogenic
580 therapy in conjunction with anti-PD-1 therapy further promotes vascular normalisation
581 mediated by $CD4^+$ T cells [16]. Recently, biomarkers for response to systemic therapies in
582 advanced HCC have been developed. Haber *et al.* found that tumours expressing high amounts
583 of an 11-gene signature (IFNAP) captured a unique immune microenvironment characterised
584 by a high gene expression of activated $CD4^+$ memory T cells, M1 macrophages, and plasma
585 cells. This novel signature predicted response and survival in patients treated in the first-line
586 setting with anti-PD1 monotherapy [60]. However, this study did not incorporate spatial analyses
587 to determine immune cell interactions within the immune microenvironment captured by the
588 IFNAP gene signature.

589

590 There are notable limitations to our study. Single-cell sequencing of TILs in HCC has identified
591 eleven unique subsets: five $CD8^+$ and six $CD4^+$ T cell clusters including naïve, effector, and
592 exhausted T cells, and mucosal-associated invariant T (MAIT) cells [52]. We were unable to
593 identify some of these subsets (undefined lymphocytes and undefined non-lymphocyte
594 immune cells) due to constraints on the number of markers that can be included in a single
595 IMC panel. Cell segmentation can become problematic when defining single cells sectioned
596 from a three-dimensional organ. As such, cluster 44 was first identified as a single cell rather
597 than two discrete closely interacting cells. This issue was resolved by examining representative

images to confirm the presence of two discrete cells. Functionality of the PVM population was inferred by *in silico* analysis, rather than single cell analysis or cell isolation and culture experiments *ex vivo*. Finally, our sample size was small. Correlations with prognostic and clinicopathological data were performed but no associations were found, perhaps related to the limited sample size.

In summary, our study has identified a novel myeloid population in HCC characteristic of PVMs, and identified several immune cell and vascular neighbourhood interactions occurring more commonly within HCC tumours. Using IMC, we were able to comprehensively immunophenotype and spatially map the immune landscape of human HCC tumour and adjacent non-tumour tissue. Further studies are required to evaluate the function of these immune cells, their effect on immune-mediated tumour control and therapeutic responses, and their role in hepatocarcinogenesis and HCC progression.

Acknowledgements

Assistance with the study: We gratefully acknowledge the subsidised access to Sydney Cytometry and thank the support staff in this core facility for their assistance. We thank the Australian Centre for Microscopy & Microanalysis at the University of Sydney for their assistance with this work.

Presentations: Preliminary data were presented at the 2023 EASL Liver Cancer Summit (Estoril, Portugal); 2023 CYTO (Montreal, Canada); and GESA AGW (Brisbane, Australia).

References

1. Sung H, Ferlay J, Siegel RL, et al. Global Cancer Statistics 2020: GLOBOCAN Estimates of Incidence and Mortality Worldwide for 36 Cancers in 185 Countries. *CA Cancer J Clin*. May 2021;71(3):209-249. doi:10.3322/caac.21660
2. Llovet JM, Kelley RK, Villanueva A, et al. Hepatocellular carcinoma. *Nat Rev Dis Primers*. Jan 21 2021;7(1):6. doi:10.1038/s41572-020-00240-3
3. Siegel RL, Miller KD, Fuchs HE, Jemal A. Cancer statistics, 2022. *CA Cancer J Clin*. Jan 2022;72(1):7-33. doi:10.3322/caac.21708
4. Amicone L, Marchetti A. Microenvironment and tumor cells: two targets for new molecular therapies of hepatocellular carcinoma. *Transl Gastroenterol Hepatol*. 2018;3:24. doi:10.21037/tgh.2018.04.05
5. Finn RS, Qin S, Ikeda M, et al. Atezolizumab plus Bevacizumab in Unresectable Hepatocellular Carcinoma. *The New England journal of medicine*. May 14 2020;382(20):1894-1905. doi:10.1056/NEJMoa1915745
6. Abou-Alfa GK, Lau G, Kudo M, et al. Tremelimumab plus Durvalumab in Unresectable Hepatocellular Carcinoma. *NEJM Evidence*. 2022;1(8)doi:10.1056/EVIDoa2100070
7. Ren Z, Xu J, Bai Y, et al. Sintilimab plus a bevacizumab biosimilar (IBI305) versus sorafenib in unresectable hepatocellular carcinoma (ORIENT-32): a randomised, open-label, phase 2–3 study. *The Lancet Oncology*. 2021;22(7):977-990. doi:10.1016/s1470-2045(21)00252-7
8. Ringelhan M, Pfister D, O'Connor T, Pikarsky E, Heikenwalder M. The immunology of hepatocellular carcinoma. *Nature immunology*. Mar 2018;19(3):222-232. doi:10.1038/s41590-018-0044-z
9. Aliya S, Lee H, Alhammadi M, Umapathi R, Huh YS. An Overview on Single-Cell Technology for Hepatocellular Carcinoma Diagnosis. *International journal of molecular sciences*. Jan 26 2022;23(3)doi:10.3390/ijms23031402
10. Yamaguchi S, Tomomatsu N, Kagoshima M, Okumoto T, Komatsu H. Effects of Y-24180, a receptor antagonist to platelet-activating factor, on allergic cutaneous eosinophilia in mice. *Life sciences*. 1999;64(11):PL139-44. doi:10.1016/s0024-3205(99)00024-7
11. Morse MA, Sun W, Kim R, et al. The Role of Angiogenesis in Hepatocellular Carcinoma. *Clin Cancer Res*. Feb 1 2019;25(3):912-920. doi:10.1158/1078-0432.CCR-18-1254
12. Liu K, Dennis C, Prince DS, et al. Vessels that encapsulate tumour clusters vascular pattern in hepatocellular carcinoma. *JHEP Rep*. Aug 2023;5(8):100792. doi:10.1016/j.jhepr.2023.100792
13. Yamaguchi R, Yano H, Iemura A, Ogasawara S, Haramaki M, Kojiro M. Expression of vascular endothelial growth factor in human hepatocellular carcinoma. *Hepatology*. Jul 1998;28(1):68-77. doi:10.1002/hep.510280111
14. Kaseb AO, Hanbali A, Cotant M, Hassan MM, Wollner I, Philip PA. Vascular endothelial growth factor in the management of hepatocellular carcinoma: a review of literature. *Cancer*. Nov 1 2009;115(21):4895-906. doi:10.1002/cncr.24537
15. Tian L, Goldstein A, Wang H, et al. Mutual regulation of tumour vessel normalization and immunostimulatory reprogramming. *Nature*. Apr 13 2017;544(7649):250-254. doi:10.1038/nature21724
16. Shigeta K, Datta M, Hato T, et al. Dual Programmed Death Receptor-1 and Vascular Endothelial Growth Factor Receptor-2 Blockade Promotes Vascular Normalization and Enhances Antitumor Immune Responses in Hepatocellular Carcinoma. *Hepatology*. Apr 2020;71(4):1247-1261. doi:10.1002/hep.30889
17. Ferguson AL, Sharman AR, Allen RO, et al. High-Dimensional and Spatial Analysis Reveals Immune Landscape-Dependent Progression in Cutaneous Squamous Cell Carcinoma. *Clin Cancer Res*. Nov 1 2022;28(21):4677-4688. doi:10.1158/1078-0432.CCR-22-1332
18. Catena R, Montuenga LM, Bodenmiller B. Ruthenium counterstaining for imaging mass cytometry. *The Journal of pathology*. Apr 2018;244(4):479-484. doi:10.1002/path.5049

670 19. Hewavisenti R, Ferguson A, Wang K, et al. CD103+ tumor-resident CD8+ T cell numbers
671 underlie improved patient survival in oropharyngeal squamous cell carcinoma. *J Immunother Cancer*.
672 Jun 2020;8(1)doi:10.1136/jitc-2019-000452
673 20. Hewavisenti RV, Ferguson AL, Gasparini G, et al. Tissue-resident regulatory T cells
674 accumulate at human barrier lymphoid organs. *Immunology and cell biology*. Sep 2021;99(8):894-
675 906. doi:10.1111/imcb.12481
676 21. Schindelin J, Arganda-Carreras I, Frise E, et al. Fiji: an open-source platform for biological-
677 image analysis. *Nat Methods*. Jun 28 2012;9(7):676-82. doi:10.1038/nmeth.2019
678 22. Berg S, Kutra D, Kroeger T, et al. ilastik: interactive machine learning for (bio)image analysis.
679 *Nat Methods*. Dec 2019;16(12):1226-1232. doi:10.1038/s41592-019-0582-9
680 23. *R: A language and environment for statistical computing*. R Foundation for Statistical
681 Computing; 2021. https://www.R-project.org/
682 24. Ashhurst TM, Marsh-Wakefield F, Putri GH, et al. Integration, exploration, and analysis of
683 high-dimensional single-cell cytometry data using Spectre. *Cytometry Part A : the journal of the*
684 *International Society for Analytical Cytology*. Mar 2022;101(3):237-253. doi:10.1002/cyto.a.24350
685 25. Samusik N, Good Z, Spitzer MH, Davis KL, Nolan GP. Automated mapping of phenotype space
686 with single-cell data. *Nat Methods*. Jun 2016;13(6):493-6. doi:10.1038/nmeth.3863
687 26. Clarke KR, Somerfield PJ, Gorley RN. Testing of null hypotheses in exploratory community
688 analyses: similarity profiles and biota-environment linkage. *Journal of Experimental Marine Biology*
689 *and Ecology*. 2008;366(1-2):56-69. doi:10.1016/j.jembe.2008.07.009
690 27. Marsh-Wakefield F, Juillard P, Ashhurst TM, et al. Peripheral B-cell dysregulation is
691 associated with relapse after long-term quiescence in patients with multiple sclerosis. *Immunology*
692 *and cell biology*. Jul 2022;100(6):453-467. doi:10.1111/imcb.12552
693 28. Rohart F, Gautier B, Singh A, Le Cao KA. mixOmics: An R package for 'omics feature selection
694 and multiple data integration. *PLoS Comput Biol*. Nov 2017;13(11):e1005752.
695 doi:10.1371/journal.pcbi.1005752
696 29. Lu Y, Yang A, Quan C, et al. A single-cell atlas of the multicellular ecosystem of primary and
697 metastatic hepatocellular carcinoma. *Nat Commun*. Aug 6 2022;13(1):4594. doi:10.1038/s41467-
698 022-32283-3
699 30. Zhang Y, Liu T, Hu X, et al. CellCall: integrating paired ligand-receptor and transcription factor
700 activities for cell-cell communication. *Nucleic Acids Res*. Sep 7 2021;49(15):8520-8534.
701 doi:10.1093/nar/gkab638
702 31. Anderson MJ. A new method for non-parametric multivariate analysis of variance. *Austral*
703 *Ecol*. Feb 2001;26(1):32-46. doi:DOI 10.1046/j.1442-9993.2001.01070.x
704 32. *vegan: Community Ecology Package*. 2019. https://CRAN.R-project.org/package=vegan
705 33. *pairwiseAdonis: Pairwise Multilevel Comparison using Adonis*. 2017.
706 https://github.com/pmartinezarbizu/pairwiseAdonis
707 34. *RVAideMemoire: Testing and Plotting Procedures for Biostatistics*. 2021. https://CRAN.R-
708 project.org/package=RVAideMemoire
709 35. Gide TN, Silva IP, Quek C, et al. Close proximity of immune and tumor cells underlies
710 response to anti-PD-1 based therapies in metastatic melanoma patients. *Oncoimmunology*.
711 2020;9(1):1659093. doi:10.1080/2162402x.2019.1659093
712 36. Harney AS, Arwert EN, Entenberg D, et al. Real-Time Imaging Reveals Local, Transient
713 Vascular Permeability, and Tumor Cell Intravasation Stimulated by TIE2hi Macrophage-Derived
714 VEGFA. *Cancer Discov*. Sep 2015;5(9):932-43. doi:10.1158/2159-8290.CD-15-0012
715 37. Lewis CE, Harney AS, Pollard JW. The Multifaceted Role of Perivascular Macrophages in
716 Tumors. *Cancer cell*. Jul 11 2016;30(1):18-25. doi:10.1016/j.ccell.2016.05.017
717 38. Lapenna A, De Palma M, Lewis CE. Perivascular macrophages in health and disease. *Nature*
718 *reviews Immunology*. Nov 2018;18(11):689-702. doi:10.1038/s41577-018-0056-9

719 39. Marsh-Wakefield F, Ferguson AL, Liu K, Santhakumar C, McCaughan G, Palendira U.
720 Approaches to spatially resolving the tumour immune microenvironment of hepatocellular
721 carcinoma. *Ther Adv Med Oncol*. 2022;14:17588359221113270. doi:10.1177/17588359221113270
722 40. Wang Y, Wang P, Zhang Z, Zhou J, Fan J, Sun Y. Dissecting the tumor ecosystem of liver
723 cancers in the single-cell era. *Hepatol Commun*. Sep 1
724 2023;7(9)doi:10.1097/HC9.0000000000000248
725 41. Haniffa M, Ginhoux F, Wang XN, et al. Differential rates of replacement of human dermal
726 dendritic cells and macrophages during hematopoietic stem cell transplantation. *The Journal of*
727 *experimental medicine*. Feb 16 2009;206(2):371-85. doi:10.1084/jem.20081633
728 42. McGovern N, Schlitzer A, Gunawan M, et al. Human dermal CD14(+) cells are a transient
729 population of monocyte-derived macrophages. *Immunity*. Sep 18 2014;41(3):465-477.
730 doi:10.1016/j.immuni.2014.08.006
731 43. Yang L, Zhang Y. Tumor-associated macrophages: from basic research to clinical application.
732 *J Hematol Oncol*. Feb 28 2017;10(1):58. doi:10.1186/s13045-017-0430-2
733 44. Li X, Yao W, Yuan Y, et al. Targeting of tumour-infiltrating macrophages via CCL2/CCR2
734 signalling as a therapeutic strategy against hepatocellular carcinoma. *Gut*. Jan 2017;66(1):157-167.
735 doi:10.1136/gutjnl-2015-310514
736 45. Wu C, Lin J, Weng Y, et al. Myeloid signature reveals immune contexture and predicts the
737 prognosis of hepatocellular carcinoma. *The Journal of clinical investigation*. Sep 1 2020;130(9):4679-
738 4693. doi:10.1172/JCI135048
739 46. Kurebayashi Y, Ojima H, Tsujikawa H, et al. Landscape of immune microenvironment in
740 hepatocellular carcinoma and its additional impact on histological and molecular classification.
741 *Hepatology*. Sep 2018;68(3):1025-1041. doi:10.1002/hep.29904
742 47. Donne R, Lujambio A. The liver cancer immune microenvironment: Therapeutic implications
743 for hepatocellular carcinoma. *Hepatology*. May 1 2023;77(5):1773-1796. doi:10.1002/hep.32740
744 48. Dong P, Ma L, Liu L, et al. CD86(+)/CD206(+), Diametrically Polarized Tumor-Associated
745 Macrophages, Predict Hepatocellular Carcinoma Patient Prognosis. *International journal of*
746 *molecular sciences*. Mar 1 2016;17(3):320. doi:10.3390/ijms17030320
747 49. Sia D, Jiao Y, Martinez-Quetglas I, et al. Identification of an Immune-specific Class of
748 Hepatocellular Carcinoma, Based on Molecular Features. *Gastroenterology*. Sep 2017;153(3):812-
749 826. doi:10.1053/j.gastro.2017.06.007
750 50. Sheng J, Zhang J, Wang L, et al. Topological analysis of hepatocellular carcinoma tumour
751 microenvironment based on imaging mass cytometry reveals cellular neighbourhood regulated
752 reversely by macrophages with different ontogeny. *Gut*. Jun 2022;71(6):1176-1191.
753 doi:10.1136/gutjnl-2021-324339
754 51. Mi H, Ho WJ, Yarchoan M, Popel AS. Multi-Scale Spatial Analysis of the Tumor
755 Microenvironment Reveals Features of Cabozantinib and Nivolumab Efficacy in Hepatocellular
756 Carcinoma. *Frontiers in immunology*. 2022;13:892250. doi:10.3389/fimmu.2022.892250
757 52. Zheng C, Zheng L, Yoo JK, et al. Landscape of Infiltrating T Cells in Liver Cancer Revealed by
758 Single-Cell Sequencing. *Cell*. Jun 15 2017;169(7):1342-1356 e16. doi:10.1016/j.cell.2017.05.035
759 53. Zhang Q, He Y, Luo N, et al. Landscape and Dynamics of Single Immune Cells in
760 Hepatocellular Carcinoma. *Cell*. Oct 31 2019;179(4):829-845 e20. doi:10.1016/j.cell.2019.10.003
761 54. Montironi C, Castet F, Haber PK, et al. Inflamed and non-inflamed classes of HCC: a revised
762 immunogenomic classification. *Gut*. Jan 2023;72(1):129-140. doi:10.1136/gutjnl-2021-325918
763 55. Matsubara T, Kanto T, Kuroda S, et al. TIE2-expressing monocytes as a diagnostic marker for
764 hepatocellular carcinoma correlates with angiogenesis. *Hepatology*. Apr 2013;57(4):1416-25.
765 doi:10.1002/hep.25965
766 56. De Palma M, Venneri MA, Galli R, et al. Tie2 identifies a hematopoietic lineage of
767 proangiogenic monocytes required for tumor vessel formation and a mesenchymal population of
768 pericyte progenitors. *Cancer cell*. Sep 2005;8(3):211-26. doi:10.1016/j.ccr.2005.08.002

769 57. Liu K, Zhang X, Xu W, et al. Targeting the vasculature in hepatocellular carcinoma treatment:
770 Starving versus normalizing blood supply. *Clin Transl Gastroenterol*. Jun 15 2017;8(6):e98.
771 doi:10.1038/ctg.2017.28
772 58. Santhakumar C, Gane EJ, Liu K, McCaughan GW. Current perspectives on the tumor
773 microenvironment in hepatocellular carcinoma. *Hepatol Int*. Dec 2020;14(6):947-957.
774 doi:10.1007/s12072-020-10104-3
775 59. Yang M, Yang C, Ma D, Li Z, Zhao W, Yang D. Single-cell analysis reveals cellular
776 reprogramming in advanced colon cancer following FOLFOX-bevacizumab treatment. *Front Oncol*.
777 2023;13:1219642. doi:10.3389/fonc.2023.1219642
778 60. Haber PK, Castet F, Torres-Martin M, et al. Molecular Markers of Response to Anti-PD1
779 Therapy in Advanced Hepatocellular Carcinoma. *Gastroenterology*. Jan 2023;164(1):72-88 e18.
780 doi:10.1053/j.gastro.2022.09.005

781

782

783 **Figure legends**

784 **Figure 1 – Experimental overview**. A) Sixteen HCC patients underwent liver resections.
785 1 mm diameter regions of non-tumour, invasive margin, and tumour were selected from each
786 patient in triplicate to create a tissue microarray. B) Sections were stained with antibodies
787 conjugated to heavy metals which were then ablated by a Helios imaging mass cytometer to
788 quantify regions. C) Ilastik software was used to define cell borders to create a mask of single
789 cells. D) R package Spectre quantified marker expression for each segmented cell across
790 regions.

791

792 **Figure 2 – Spatial environment differs between liver regions**. A) X-shift clustering was
793 used to identify 47 clusters represented by a heatmap. Each row is a different cluster, each
794 column a different marker. B) Principal component analysis (PCA) of all spatial data. Symbols
795 and colours represent a different region from individual patients. 95 % confidence interval
796 shown. A PERMANOVA with Holm's correction was performed on all parameters. C) The
797 parameters that contributed most to the variance across the first two components are shown.
798 Horizontal red dashed line represents the value if all parameters contributed equally. D) A
799 sparse partial least squares-discriminant analysis (sPLS-DA) generated a similar plot, with the
800 selected parameters for the first two components shown. A PERMANOVA with Holm's
801 correction was performed on select parameters from the first two components. E) The
802 parameters that contribute most to the differences between regions across the first two
803 components are shown. n = 16 HCC patients, each with non-tumour, invasive margin, and
804 tumour regions.

805

806 **Figure 3 – Tumour has higher densities of monocyte-derived CD11c$^+$ and CD11c$^-$**
807 **macrophage subsets compared to non-tumour regions**. A) Proportion of conventional
808 immune cells across regions. B) The density of conventional immune subsets across regions.
809 Friedman test with Dunn's multiple comparison corrections was performed. C) Log_2 fold
810 change comparing densities of monocyte-derived CD11c$^+$ and CD11c$^-$ macrophages between
811 tumour and non-tumour regions. Wilcoxon test was used. *$p<0.05$, **$p<0.01$, ***$p<0.001$.
812 n = 16 HCC patients.

813

814 **Figure 4 – Immune cell neighbours differ between non-tumour and tumour regions**. A)
815 Heatmap of CD45$^+$ clusters. Each row is a cluster, each column is a marker. B) sPLS-DA
816 comparing non-tumour to tumour regions. Symbols and colours represent a different region
817 from individual patients. 95 % confidence interval shown. C) Selected parameters for the first
818 two components are shown. Select comparisons between non-tumour and tumour
819 neighbourhood interactions (D) and densities (E). n = 16 HCC patients, each with non-tumour,
820 invasive margin, and tumour regions. A permutation student's t-test was done, p-values ≤0.1
821 are shown, mean is shown.

822

823 **Figure 5 – Cluster 44 consists of endothelial and VEGF$^+$ perivascular macrophages**. A)
824 Cluster 44 (green) location indicated between non-tumour and tumour regions from the same
825 patient. Yellow arrows point towards the location of HLA-DR$^+$ CD34$^+$ cells (yellow). B)
826 Histograms showing relative marker expression for cluster 44 (red) compared to total cells
827 (grey). C) OPAL multiplex immunohistochemistry of tumour regions. HLA-DR (red), FXIIIA
828 (green), VEGF (cyan), CD34 (purple), and DAPI (dark blue). Yellow arrows pointing to white
829 cells expressing HLA-DR, FXIIIA, and VEGF. D) Ligand-receptor communication between
830 *CD34*$^+$ endothelial cells and *VEGFA*$^+$ macrophages. 10 patients with HCC and paired non-
831 tumour and tumour regions were used.

832

833 **Figure 6 – Cluster 44 has a higher number of neighbourhood interactions with clusters 9,**
834 **3, 8, and 35 within tumour compared to non-tumour**. A) Cluster 3 (CD3$^+$ CD4$^+$ cells, white
835 arrows) and cluster 44 (CD34$^+$ HLA-DR$^+$ cells, yellow arrows) location indicated between
836 non-tumour and tumour regions. B) Cluster 9 (CD8A$^+$ cells, white arrows) and cluster 44
837 (CD34$^+$ HLA-DR$^+$ cells, yellow arrows) location indicated between non-tumour and tumour
838 regions. C) Histograms representing marker expression of cluster 3 (blue), cluster 9 (red), and
839 total cells (grey). D) Cluster 8 (CD11c$^+$ HLA-DR$^+$, yellow arrows) and cluster 44 (CD34$^+$
840 HLA-DR$^+$, white arrows) location indicated between non-tumour and tumour regions. E)
841 Cluster 35 (CD68$^+$, white arrows) and cluster 44 (CD34$^+$ HLA-DR$^+$, yellow arrows) location
842 indicated between non-tumour and tumour regions. F) Histograms representing marker
843 expression of cluster 8 (blue), cluster 35 (red), and total cells (grey). Representative non-
844 tumour and tumour regions are from the same patient.

845

846 **Figure 7 – Neighbourhood interactions between clusters 8 and 9, and clusters 35 and 45**
847 **are higher in tumour than non-tumour**. A) Cluster 8 ($CD11c^+$ $HLA\text{-}DR^+$, yellow arrows)
848 and cluster 9 ($CD8A^+$, white arrows) location indicated between non-tumour and tumour
849 regions. B) Cluster 35 ($CD14^+$ $CD68^+$, yellow arrows) and cluster 45 ($CD14^+$ $CD68^+$ $FXIIIA^+$,
850 white arrows) location indicated between non-tumour and tumour regions. C) Histograms
851 representing marker expression of cluster 45 (red) and total cells (grey). Representative non-
852 tumour and tumour regions are from the same patient.

853

854 **Figure 8 – Summary figure**. Liver resections were collected from patients with HCC to create
855 a tissue microarray. Regions include non-tumour, invasive margin, and tumour. Imaging mass
856 cytometry was done on sections with a representative image shown. Within the tumour, a
857 unique intratumoural perivascular-immune neighbourhood was identified, featuring cells as
858 described.

859

860

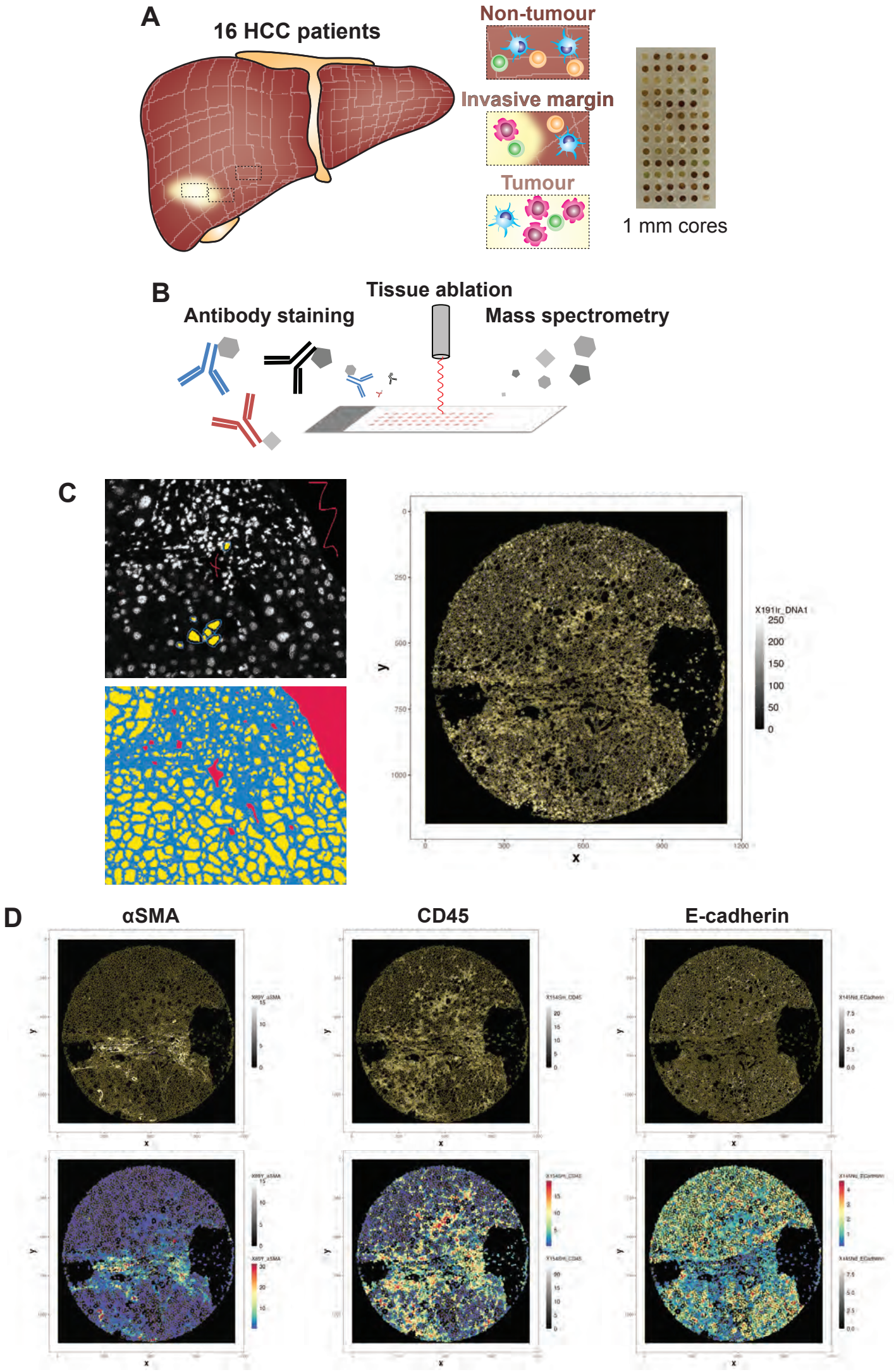
A
16 HCC patients
Non-tumour
Invasive margin
Tumour
1 mm cores
B
Tissue ablation
Antibody staining
Mass spectrometry
C
X191Ir_DNA1
250
200
150
100
50
0
y
x
D
αSMA
CD45
E-cadherin

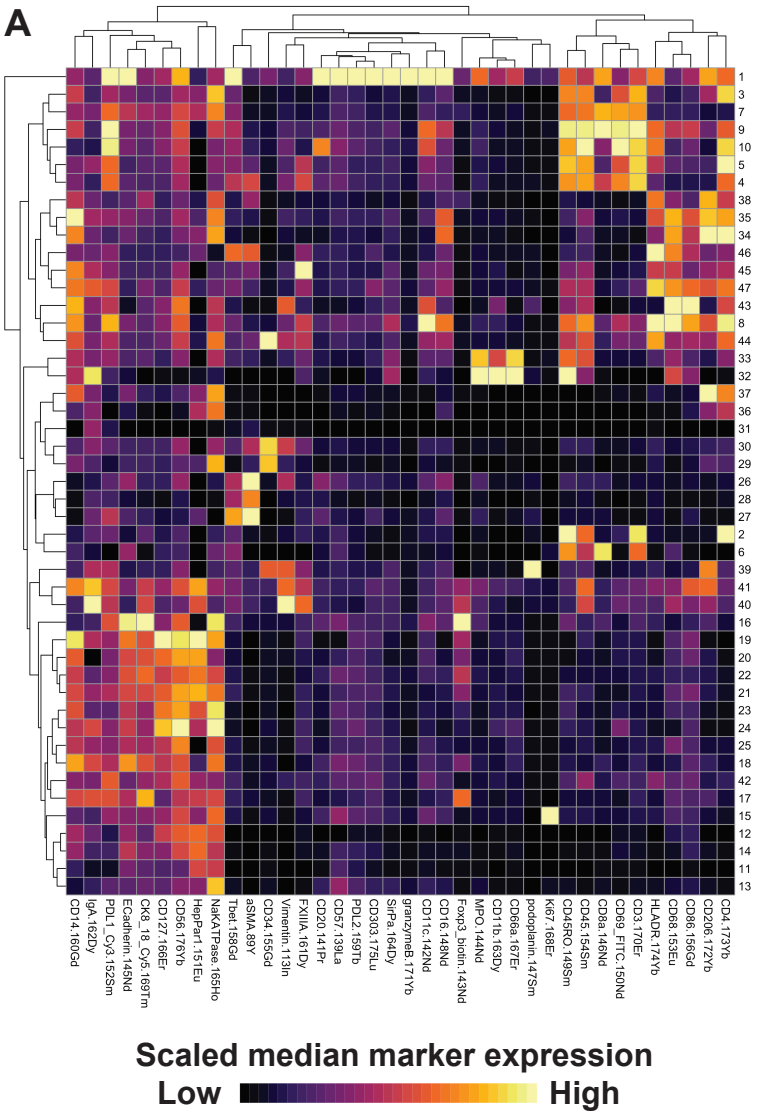

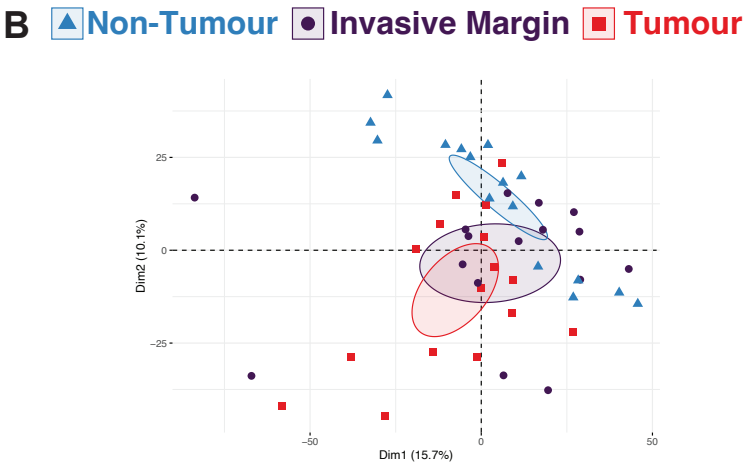

Group comparison	R^2	*P*-value
PERMANOVA	0.0700	***0.0030***
Invasive Margin vs Tumour	0.0393	0.2476
Non-Tumour vs Invasive Margin	0.0416	0.2476
Non-Tumour vs Tumour	0.0812	***0.0006***

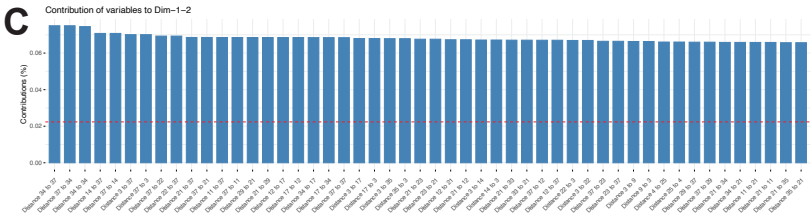

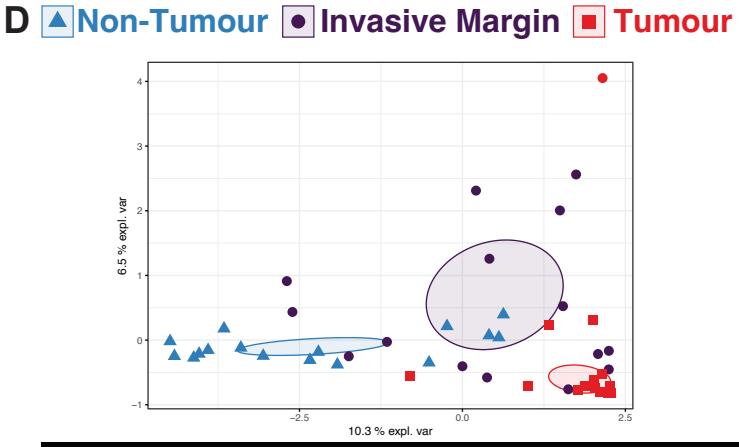

Group comparison	R^2	*P*-value
PERMANOVA	0.4362	***0.0004***
Invasive Margin vs Tumour	0.1957	***0.0008***
Non-Tumour vs Invasive Margin	0.2785	***0.0008***
Non-Tumour vs Tumour	0.5417	***0.0006***

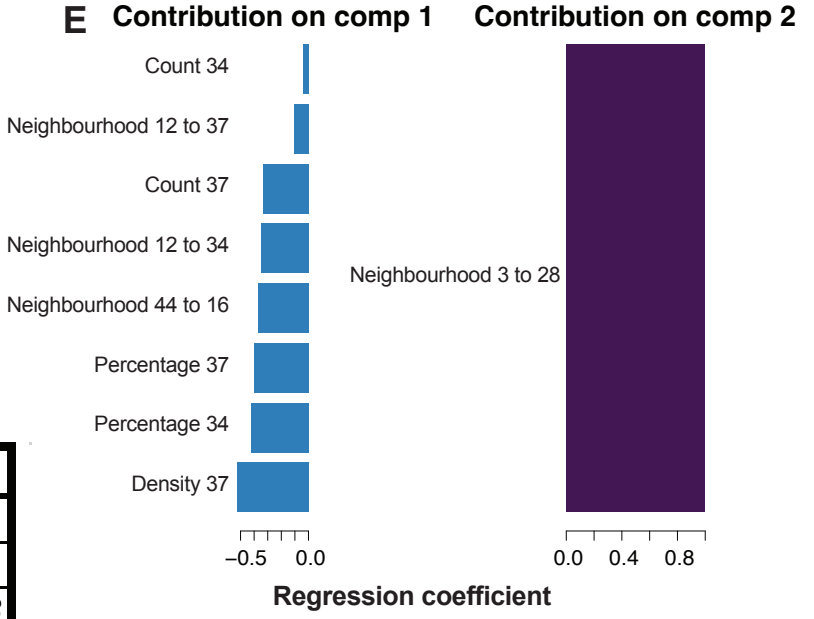

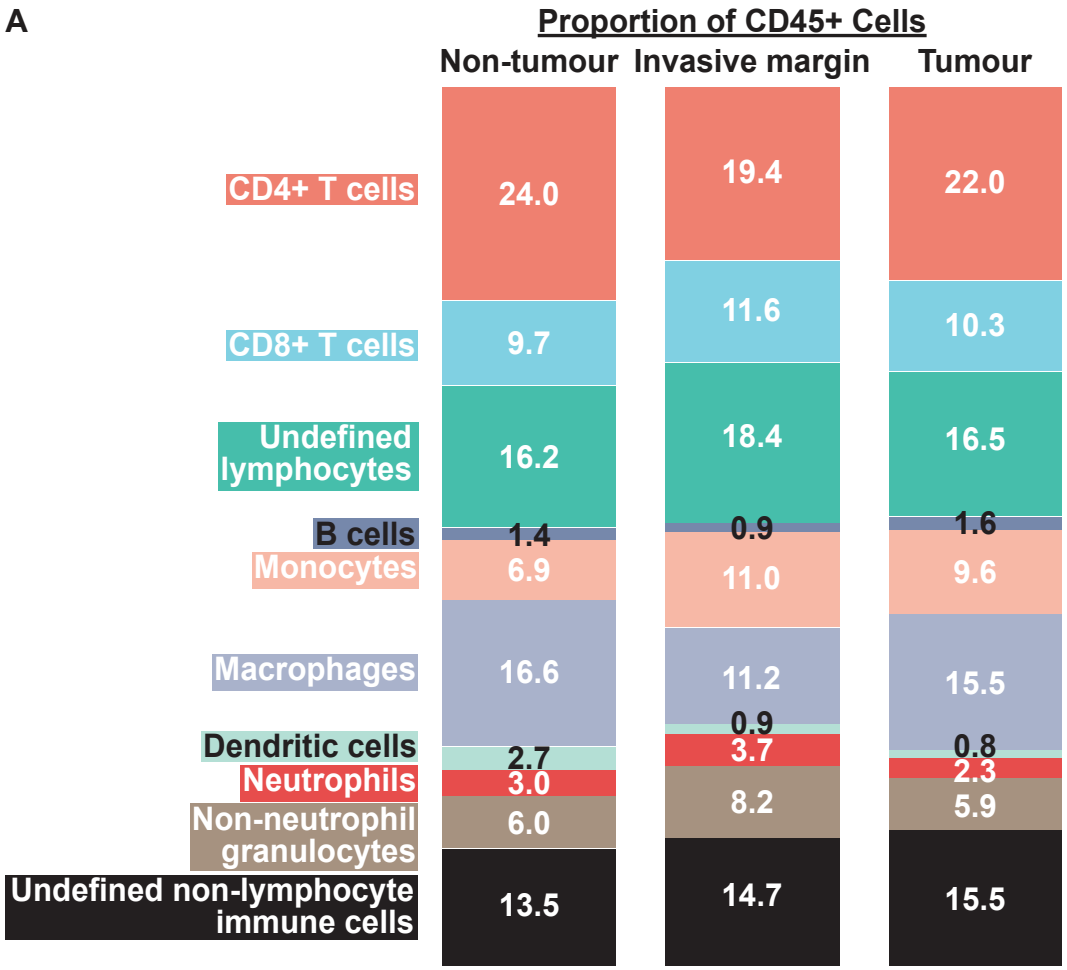
A
Proportion of CD45+ Cells
Non-tumour
Invasive margin
Tumour
CD4+ T cells
CD8+ T cells
Undefined lymphocytes
B cells
Monocytes
Macrophages
Dendritic cells
Neutrophils
Non-neutrophil granulocytes
Undefined non-lymphocyte immune cells
24.0
9.7
16.2
1.4
6.9
16.6
2.7
3.0
6.0
13.5
19.4
11.6
18.4
0.9
11.0
11.2
0.9
3.7
8.2
14.7
22.0
10.3
16.5
1.6
9.6
15.5
0.8
2.3
5.9
15.5

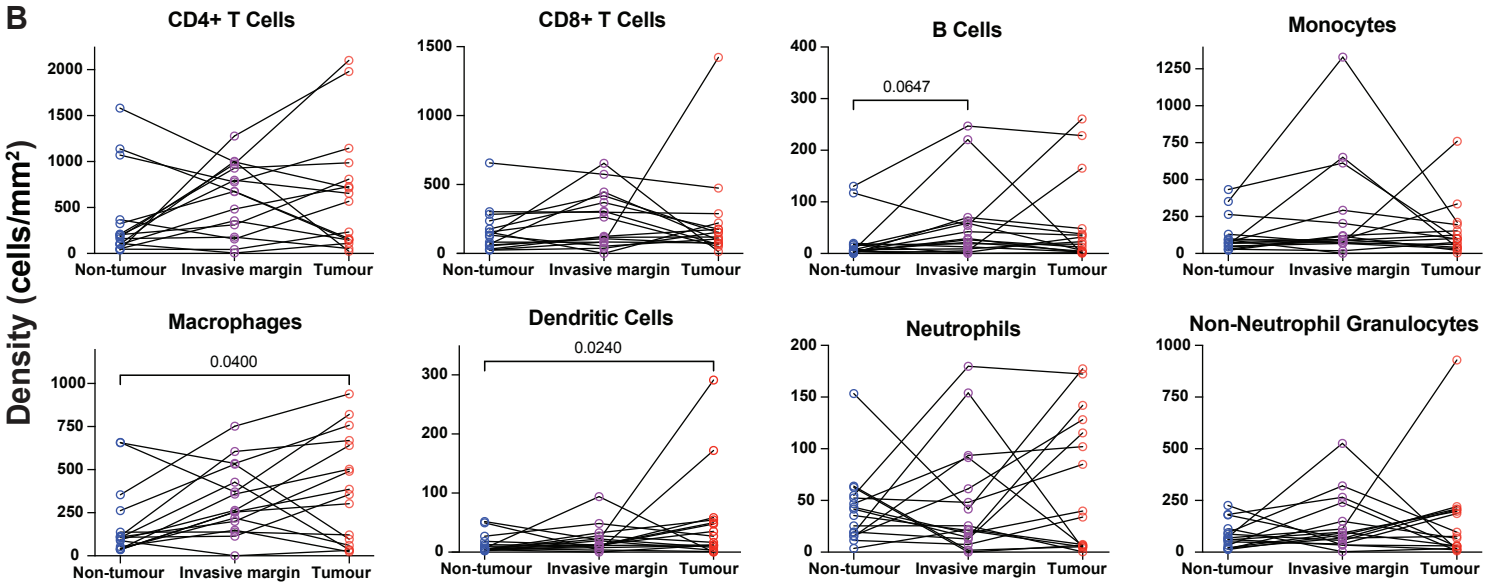
B
Density (cells/mm²)
CD4+ T Cells
CD8+ T Cells
B Cells
Monocytes
Macrophages
Dendritic Cells
Neutrophils
Non-Neutrophil Granulocytes
0.0647
0.0400
0.0240
Non-tumour
Invasive margin
Tumour

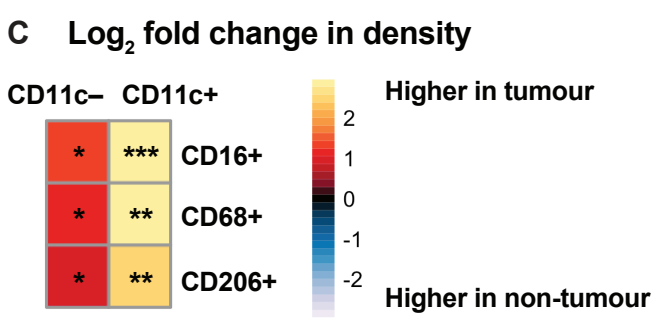
C
Log2 fold change in density
CD11c–
CD11c+
CD16+
CD68+
CD206+
*
***
**
Higher in tumour
Higher in non-tumour

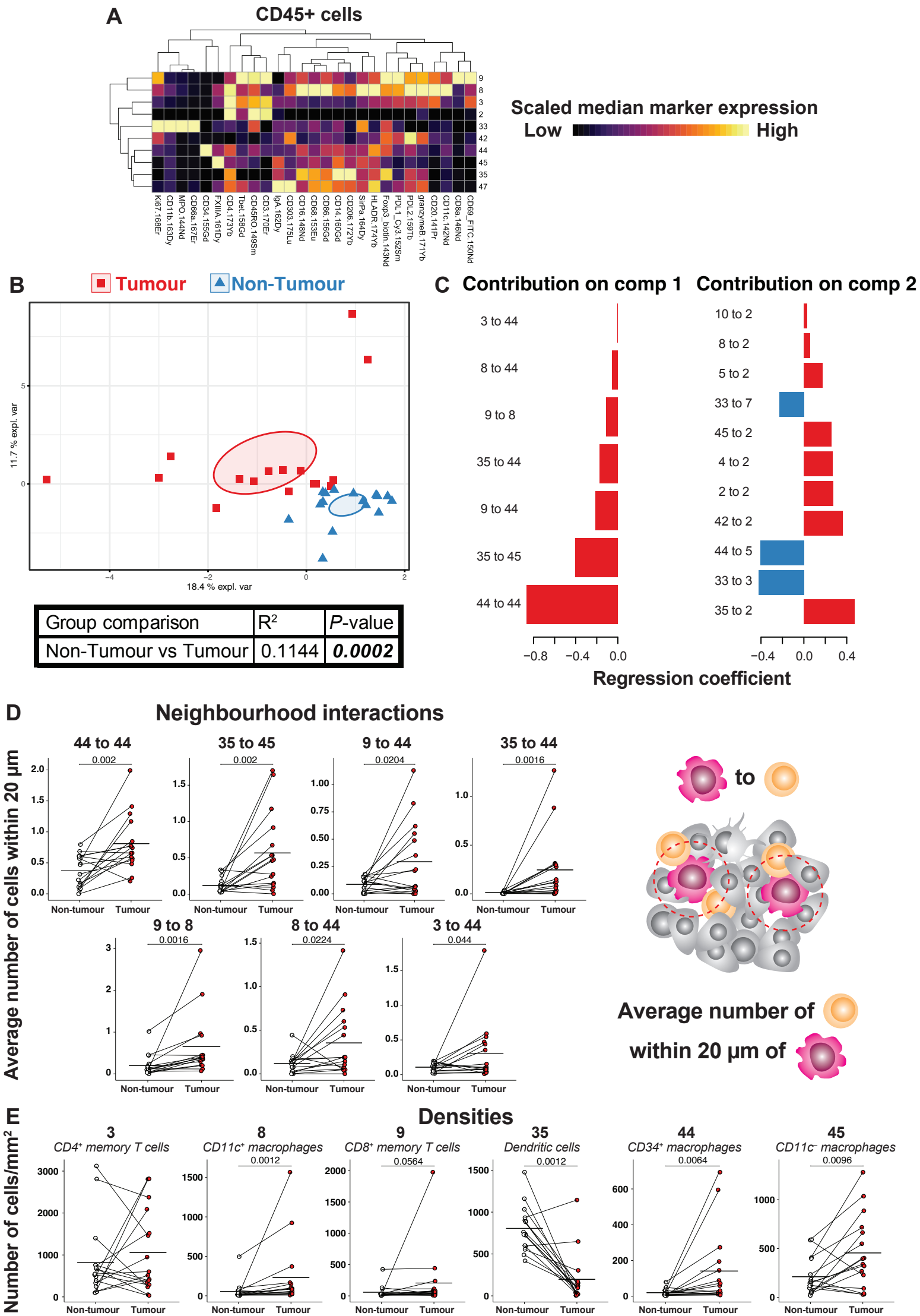

Group comparison	R^2	*P*-value
Non-Tumour vs Tumour	0.1144	***0.0002***

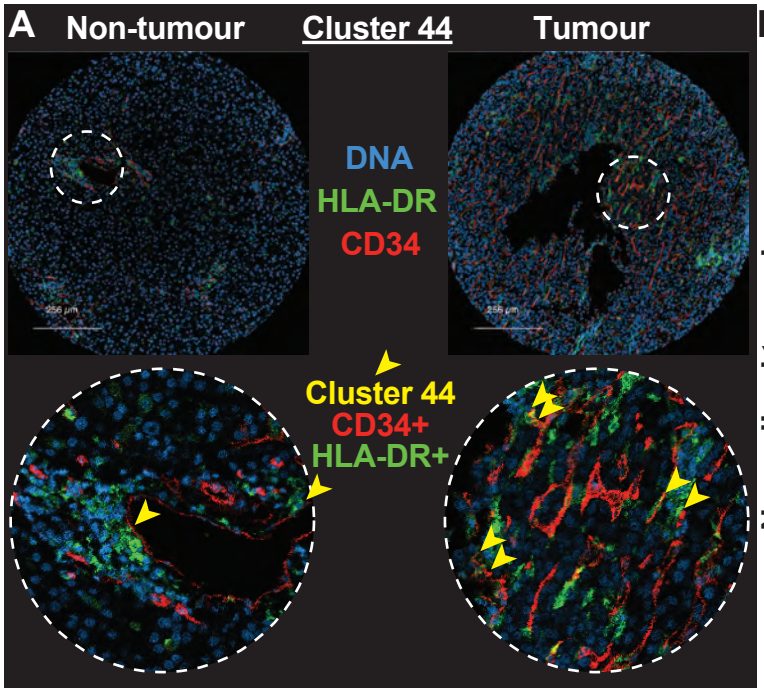

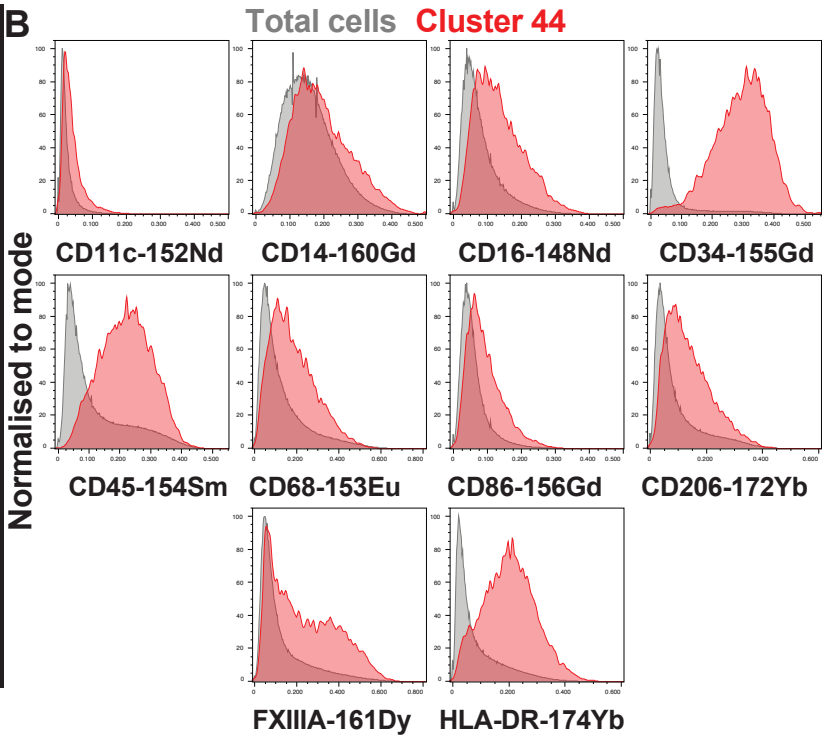

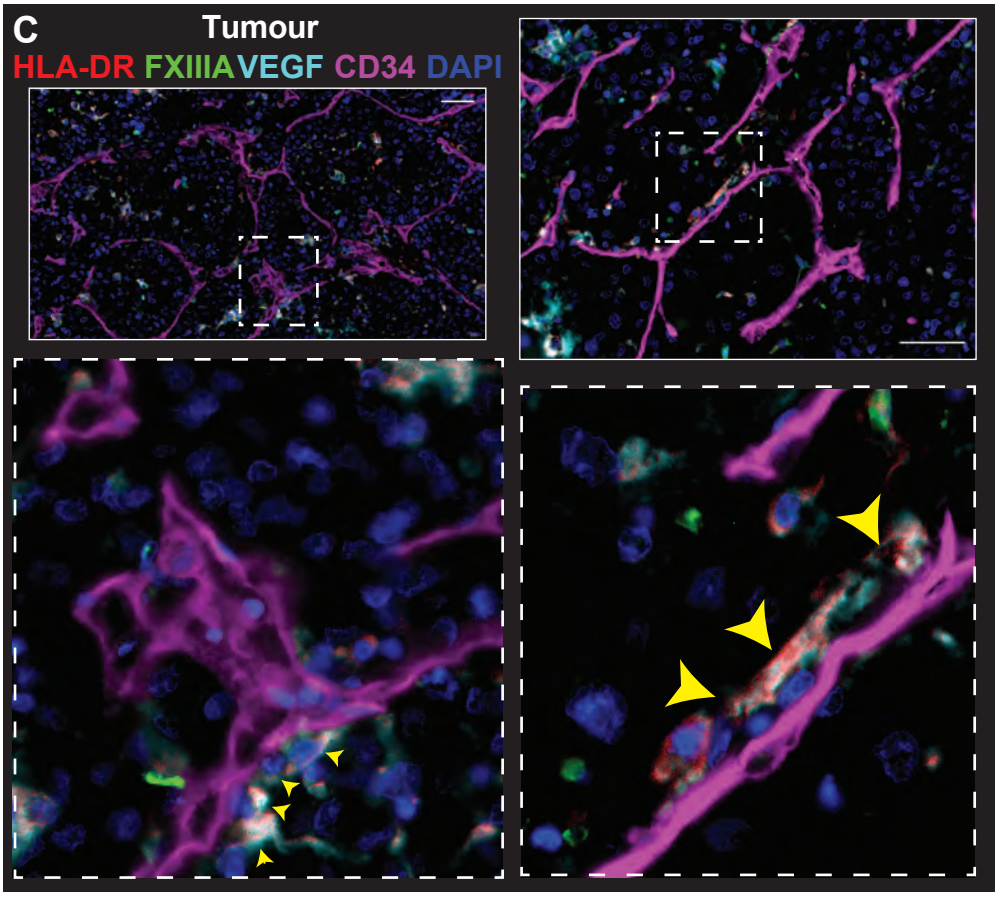

D *Cd34*⁺ endothelial cell (C48) as ligand

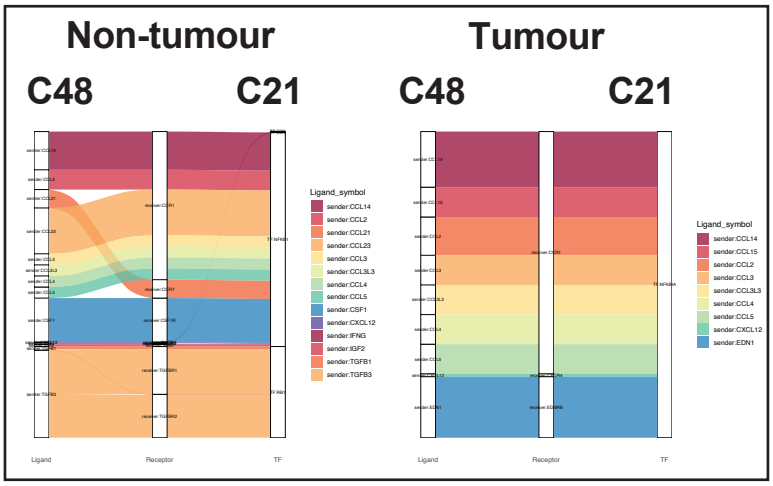

Vegfa⁺ macrophage (C21) as ligand

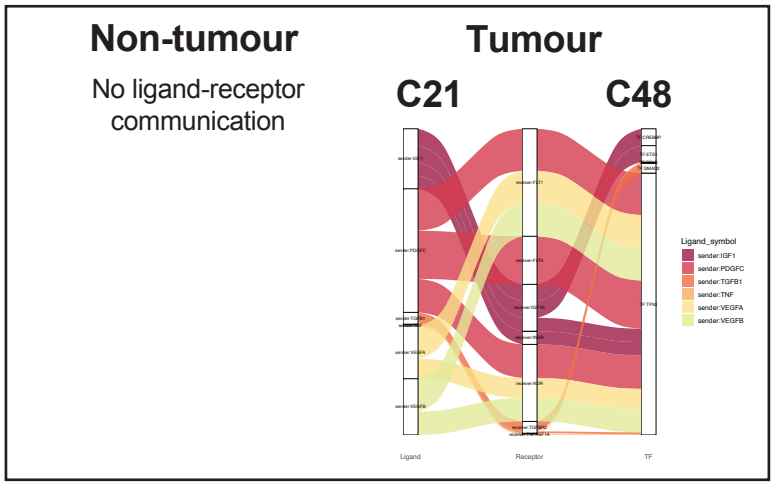

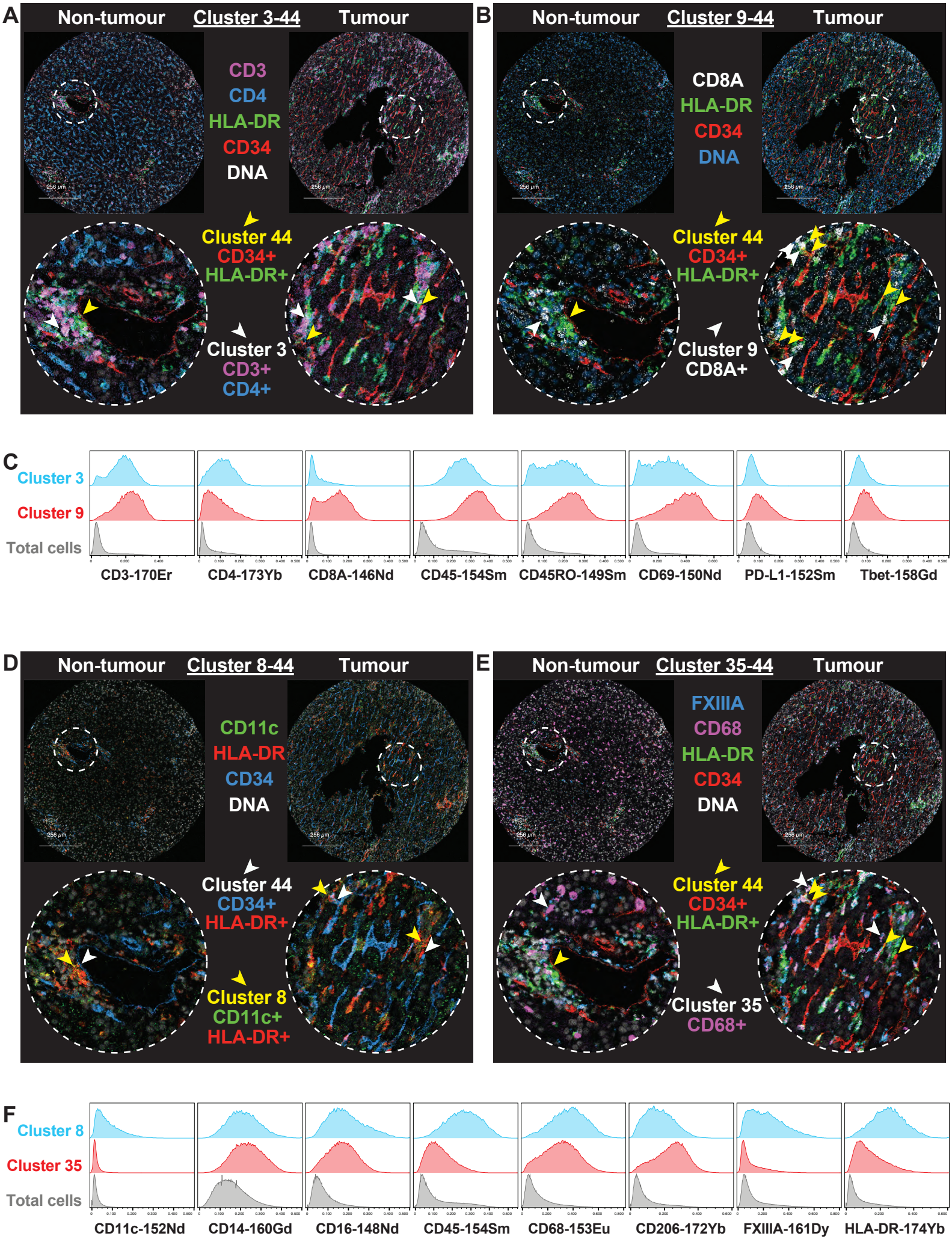
A
Non-tumour
Cluster 3-44
Tumour
CD3
CD4
HLA-DR
CD34
DNA
Cluster 44
CD34+
HLA-DR+
Cluster 3
CD3+
CD4+
B
Non-tumour
Cluster 9-44
Tumour
CD8A
HLA-DR
CD34
DNA
Cluster 44
CD34+
HLA-DR+
Cluster 9
CD8A+
C
Cluster 3
Cluster 9
Total cells
CD3-170Er
CD4-173Yb
CD8A-146Nd
CD45-154Sm
CD45RO-149Sm
CD69-150Nd
PD-L1-152Sm
Tbet-158Gd
D
Non-tumour
Cluster 8-44
Tumour
CD11c
HLA-DR
CD34
DNA
Cluster 44
CD34+
HLA-DR+
Cluster 8
CD11c+
HLA-DR+
E
Non-tumour
Cluster 35-44
Tumour
FXIIIA
CD68
HLA-DR
CD34
DNA
Cluster 44
CD34+
HLA-DR+
Cluster 35
CD68+
F
Cluster 8
Cluster 35
Total cells
CD11c-152Nd
CD14-160Gd
CD16-148Nd
CD45-154Sm
CD68-153Eu
CD206-172Yb
FXIIIA-161Dy
HLA-DR-174Yb

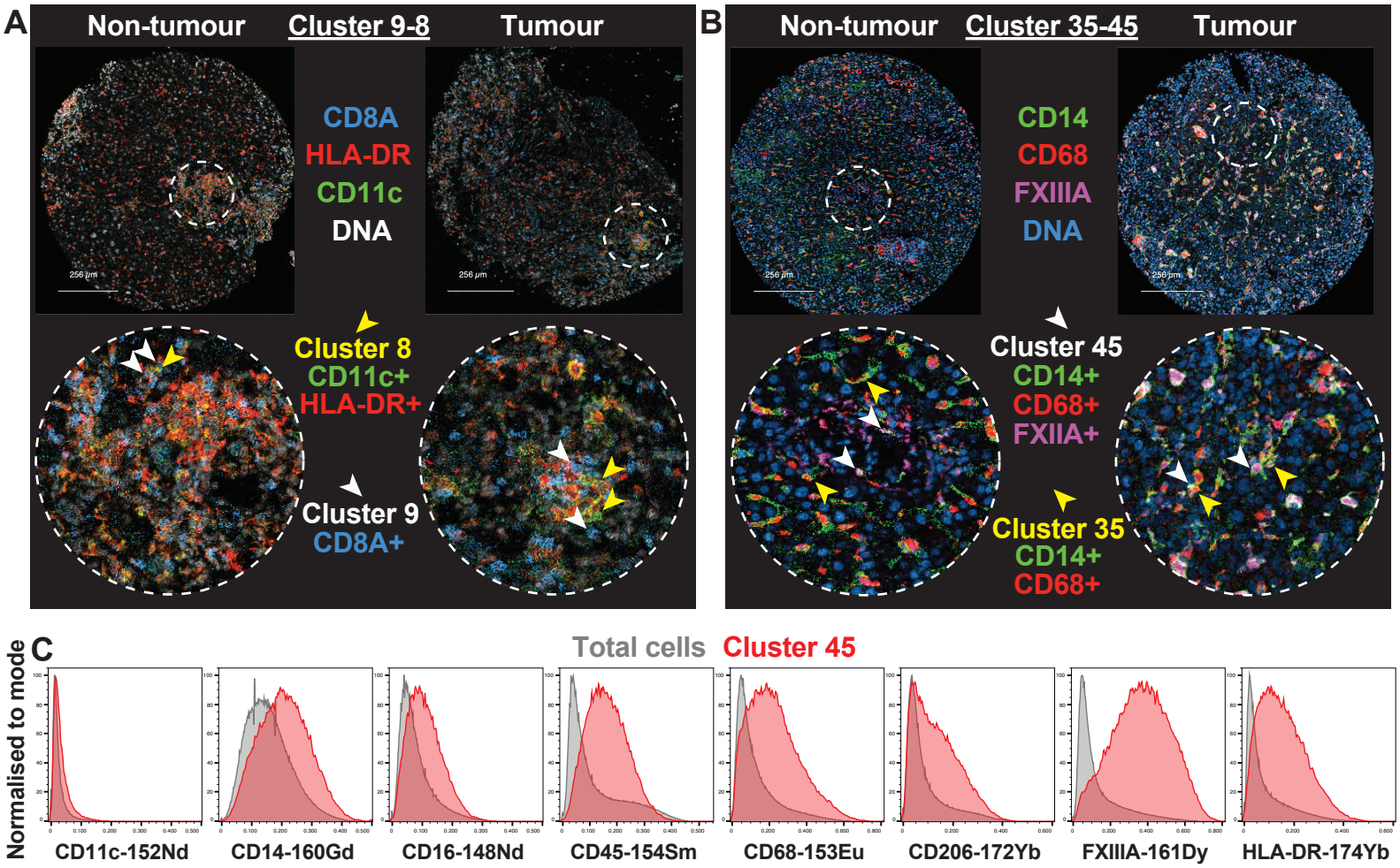
A
Non-tumour
Cluster 9-8
Tumour
CD8A
HLA-DR
CD11c
DNA
256 µm
Cluster 8
CD11c+
HLA-DR+
Cluster 9
CD8A+
B
Non-tumour
Cluster 35-45
Tumour
CD14
CD68
FXIIIA
DNA
Cluster 45
CD14+
CD68+
FXIIA+
Cluster 35
CD14+
CD68+
C
Total cells
Cluster 45
Normalised to mode
CD11c-152Nd
CD14-160Gd
CD16-148Nd
CD45-154Sm
CD68-153Eu
CD206-172Yb
FXIIIA-161Dy
HLA-DR-174Yb

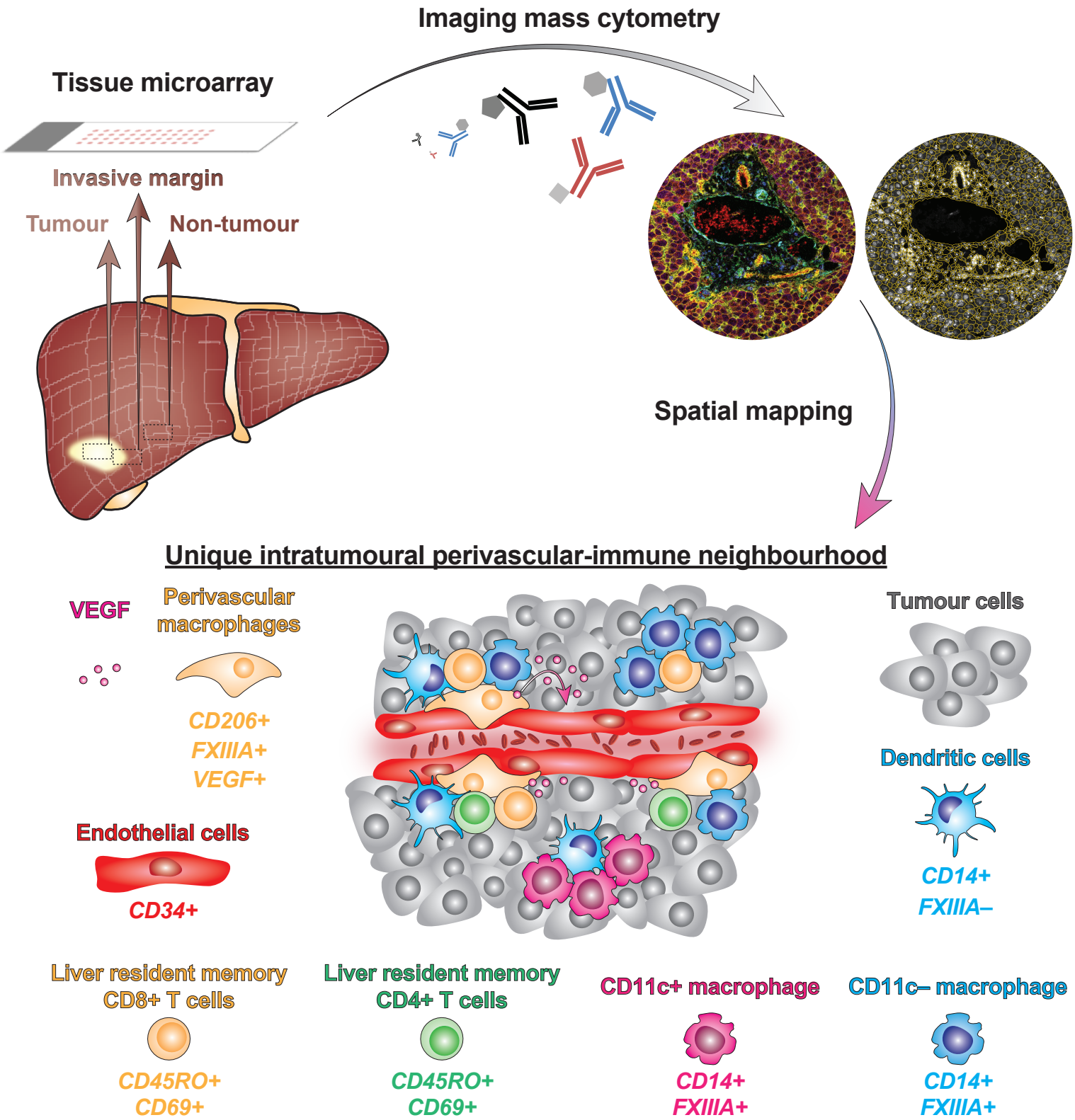
Imaging mass cytometry
Tissue microarray
Invasive margin
Tumour
Non-tumour
Spatial mapping
Unique intratumoural perivascular-immune neighbourhood
VEGF
Perivascular macrophages
CD206+
FXIIIA+
VEGF+
Endothelial cells
CD34+
Tumour cells
Dendritic cells
CD14+
FXIIIA–
Liver resident memory CD8+ T cells
CD45RO+
CD69+
Liver resident memory CD4+ T cells
CD45RO+
CD69+
CD11c+ macrophage
CD14+
FXIIIA+
CD11c– macrophage
CD14+
FXIIIA+

SUPPLEMENTARY FIGURES

Supplementary Figure 1 – Manual gating strategy of immune cell subsets. Representative gating strategy identifying immune cell subsets.

Supplementary Figure 2 – Clustering of single cells. A) Total cells were clustered using X-shift. B) The median signal intensity of CD45 was calculated for each cluster before running z-score normalisation. Red vertical line is at zero, whereby a negative cluster indicates no CD45 expression, whilst a positive value indicates CD45 expression. The blue line represents the absolute value of the smallest value, used to differentiate between $CD45^{low}$ and $CD45^{hi}$ populations. C) Cells then underwent X-shift clustering within each of the three groups ($CD45^{-}$, $CD45^{low}$, $CD45^{hi}$) resulting in 91, 36, and 18 clusters respectively. Similar clusters were then combined using the function simprof as part of the 'clustsig' R package, generating 47 clusters (20 $CD45^{+}$ clusters and 27 $CD45^{-}$ clusters). D) The number of $CD45^{+}$ clusters with ≥5 cells in each region were calculated. Clusters with <5 cells across less than a third of total regions were excluded, which removed six clusters. Heatmaps show the scaled median signal expression of each marker (columns) across each cluster (rows).

Supplementary Figure 3 – T cell and myeloid cell subset levels across regions. A) Densities of T cell subsets across regions. Friedman test with Dunn's multiple comparison corrections was done. B) Densities of $CD14^{-}$ non-monocyte-derived macrophages across regions. C) Density and proportions (% of $CD45^{+}$ cells or total cells) across myeloid cell subsets. Wilcoxon test was used.

Supplementary Figure 4 – Phenotypically similar clusters were combined. $CD45^{+}$ clusters that were phenotypically similar were combined. Representative images show each cluster (red) compared to total cells (grey).

Supplementary Figure 5 – Representative images of parameters that contributed to differences between non-tumour and tumour regions. Representative images of cluster

results on segmented data (green, dark blue, dark red dots). Images of imaging mass cytometry with markers and clusters as indicated.

Supplementary Figure 6 –T cell marker expression. A) Representative image of CD4 (red) and CD8A (green) staining. B) Plot showing cluster 3 (blue, $CD4^+$ T cells), cluster 9 (red, $CD8^+$ T cells), and total cells (grey) against CD4 and CD8 staining. C) Plots showing cluster 3 (blue, $CD4^+$ T cells), cluster 9 (red, $CD8^+$ T cells), and total cells (grey) for PD-L1 and T-bet expression.

Supplementary Figure 7 – No association between clinical parameters and tumour neighbourhood interaction. Tumour neighbourhood interactions were correlated with A) cirrhosis, B) early recurrence (<2 years), C) microvascular invasion (MVI), and D) viral-associated HCC. Permutation student's t-test.

Single cells

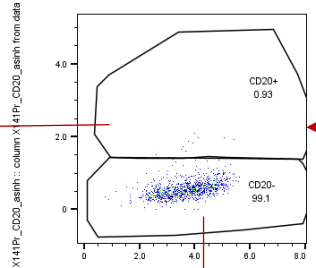

CD45+CD3-CD20+
B Cells

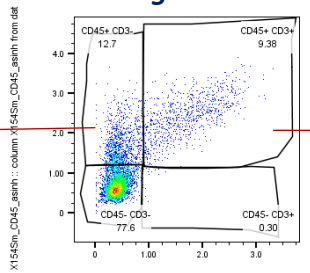

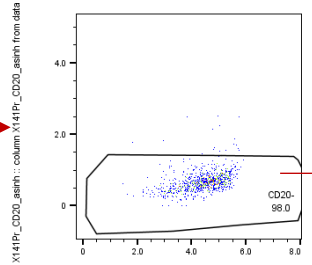

CD45+CD3+CD20-CD4+CD8+/CD45+CD3+CD20-CD4-CD8-
Undefined Lymphocytes

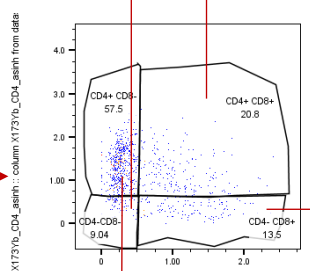

CD45+CD3+CD20-CD4-CD8+
CD8 T Cells

CD45+CD3+CD20-CD4+CD8-
CD4 T Cells

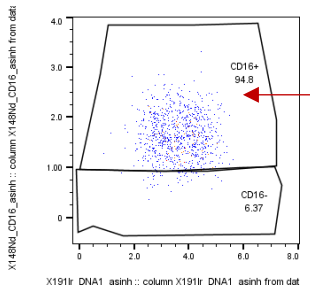

CD45+CD3-CD20-CD14+HLADR+FXIIIa+CD11c-CD16+
CD16+ Monocyte Derived CD11c- Macrophages

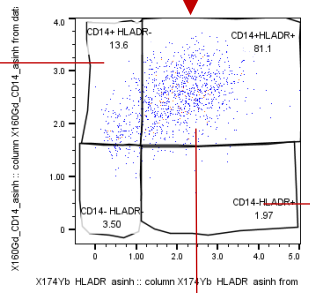

CD45+CD3-CD20-CD14+HLADR-
Monocytes

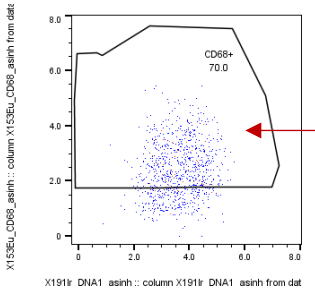

CD45+CD3-CD20-CD14+HLADR+FXIIIa+CD11c-CD68+
CD68+ Monocyte Derived CD11c- Macrophages

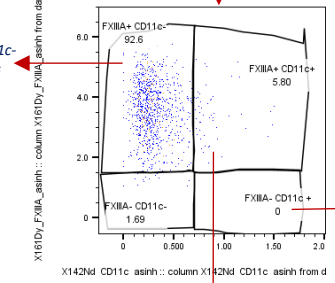

CD45+CD3-CD20-CD14+HLADR+FXIIIa+CD11c-
Monocyte Derived CD11c- Macrophages

CD45+CD3-CD20-CD14+HLADR+FXIIIa-CD11c+
Monocyte Derived CD11c+ Dendritic Cells

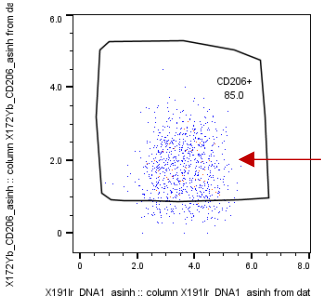

CD45+CD3-CD20-CD14+HLADR+FXIIIa+CD11c-CD206+
CD206+ Monocyte Derived CD11c- Macrophages

CD45+CD3-CD20-CD14+HLADR+FXIIIa+CD11c+
Monocyte Derived CD11c+ Macrophages

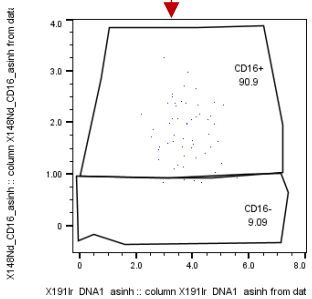

CD45+CD3-CD20-CD14+HLADR+FXIIIa+CD11c+CD16+
CD16+ Monocyte Derived CD11c+ Macrophages

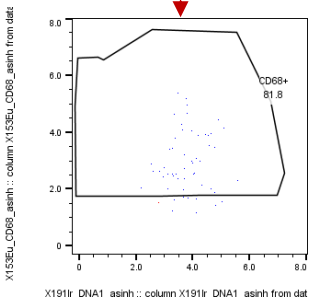

CD45+CD3-CD20-CD14+HLADR+FXIIIa+CD11c+CD68+
CD68+ Monocyte Derived CD11c+ Macrophages

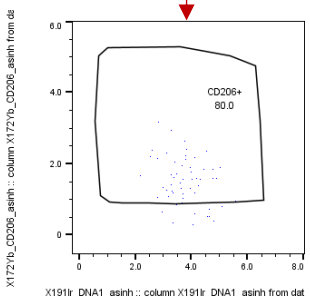

CD45+CD3-CD20-CD14+HLADR+FXIIIa+CD11c+CD206+
CD206+ Monocyte Derived CD11c+ Macrophages

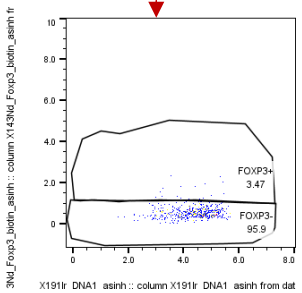

CD45+CD3+CD20-CD4+CD8-FOXP3+
FOXP3+ CD4 T Cells

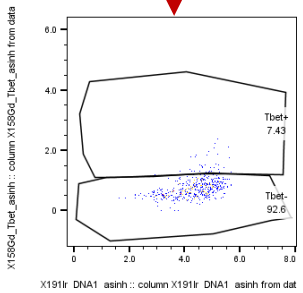

CD45+CD3+CD20-CD4+CD8-FOXP3-Tbet+
Tbet + CD4 T Cells

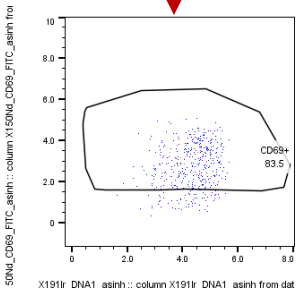

CD45+CD3+CD20-CD4+CD8-FOXP3-Tbet-CD69+
CD69+ CD4 T Cells

CD45+CD3-CD20-CD14-HLADR+FXIIIa+CD11c-
Non-Monocyte Derived CD11c- Macrophages

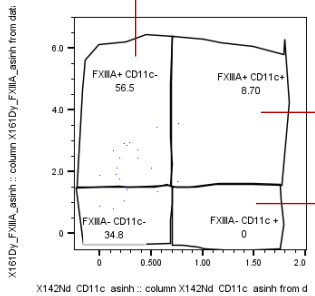

CD45+CD3-CD20-CD14-HLADR+FXIIIa+CD11c+
Non-Monocyte Derived CD11c+ Macrophages

CD45+CD3-CD20-CD14-HLADR+FXIIIa-CD11c+
Non-Monocyte Derived CD11c+ Dendritic Cells

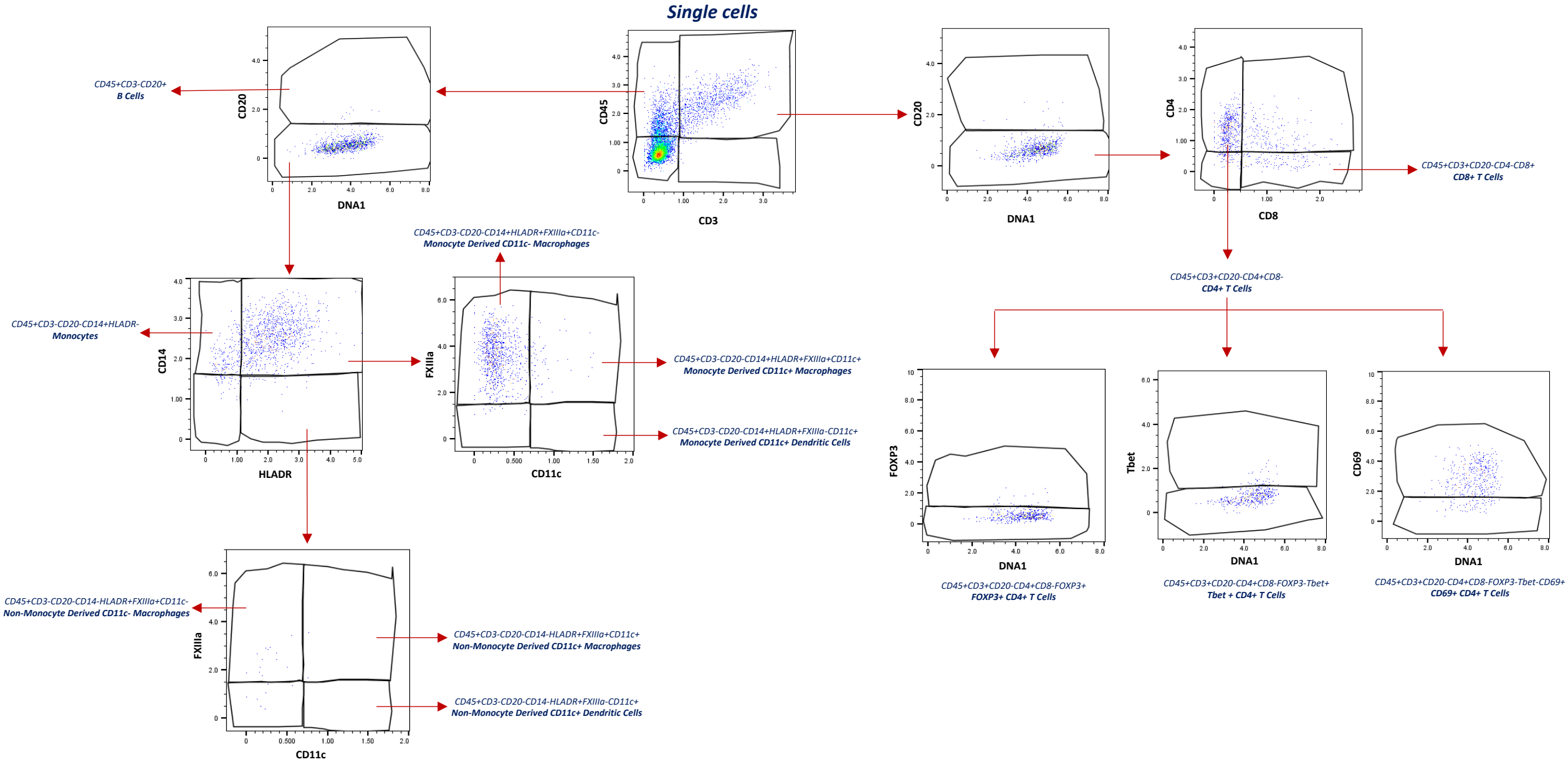
Single cells
CD45
CD3
CD20
DNA1
CD45+CD3-CD20+
B Cells
CD4
CD8
CD45+CD3+CD20-CD4-CD8+
CD8+ T Cells
CD45+CD3+CD20-CD4+CD8-
CD4+ T Cells
CD14
HLADR
CD45+CD3-CD20-CD14+HLADR-
Monocytes
FXIIIa
CD11c
CD45+CD3-CD20-CD14+HLADR+FXIIIa+CD11c-
Monocyte Derived CD11c- Macrophages
CD45+CD3-CD20-CD14+HLADR+FXIIIa+CD11c+
Monocyte Derived CD11c+ Macrophages
CD45+CD3-CD20-CD14+HLADR+FXIIIa-CD11c+
Monocyte Derived CD11c+ Dendritic Cells
CD45+CD3-CD20-CD14-HLADR+FXIIIa+CD11c-
Non-Monocyte Derived CD11c- Macrophages
CD45+CD3-CD20-CD14-HLADR+FXIIIa+CD11c+
Non-Monocyte Derived CD11c+ Macrophages
CD45+CD3-CD20-CD14-HLADR+FXIIIa-CD11c+
Non-Monocyte Derived CD11c+ Dendritic Cells
FOXP3
CD45+CD3+CD20-CD4+CD8-FOXP3+
FOXP3+ CD4+ T Cells
Tbet
CD45+CD3+CD20-CD4+CD8-FOXP3-Tbet+
Tbet + CD4+ T Cells
CD69
CD45+CD3+CD20-CD4+CD8-FOXP3-Tbet-CD69+
CD69+ CD4+ T Cells

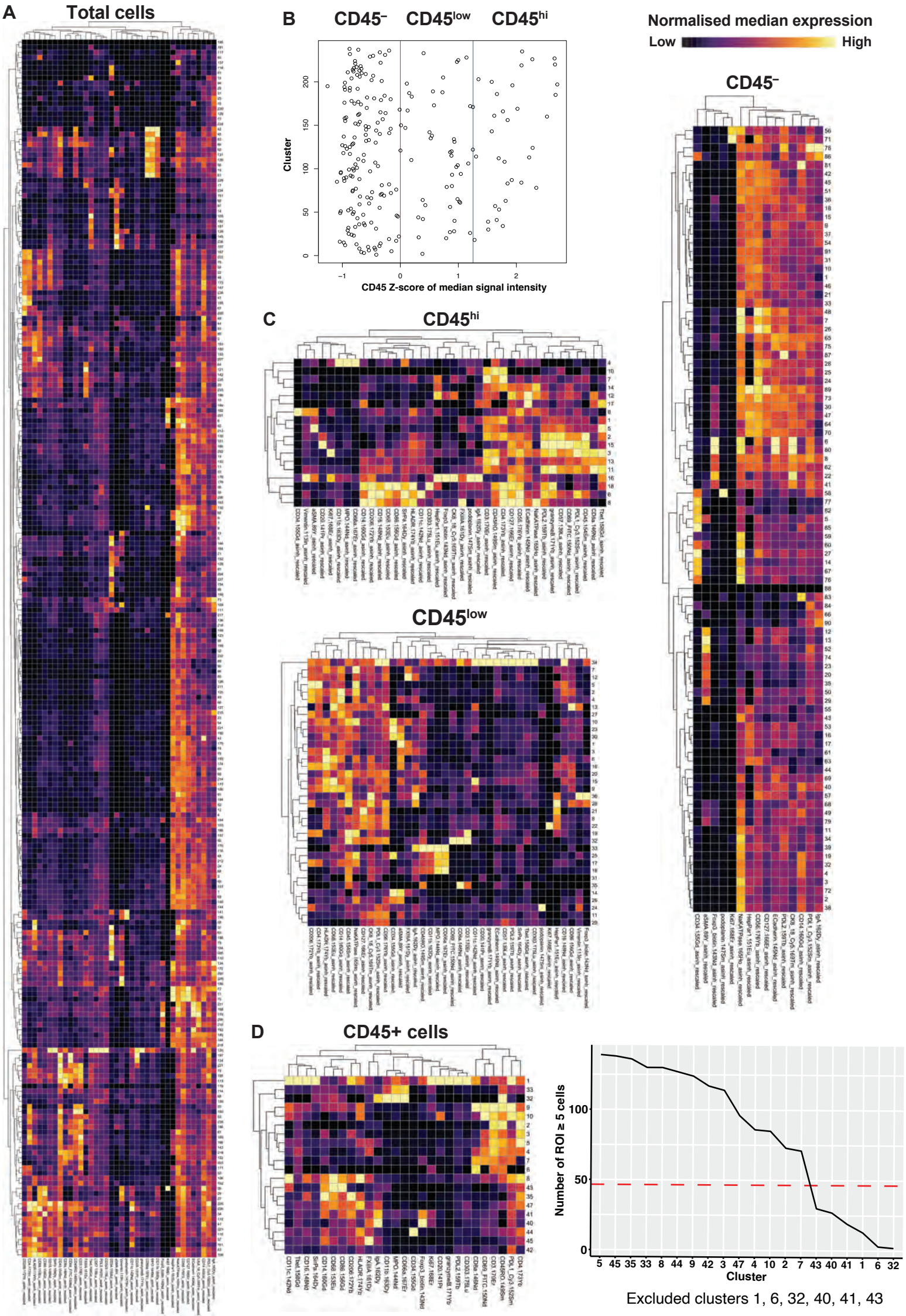
A
Total cells
B
CD45⁻
CD45low
CD45hi
Cluster
CD45 Z-score of median signal intensity
Normalised median expression
Low
High
CD45⁻
C
CD45hi
CD45low
D
CD45+ cells
Number of ROI ≥ 5 cells
Cluster
Excluded clusters 1, 6, 32, 40, 41, 43

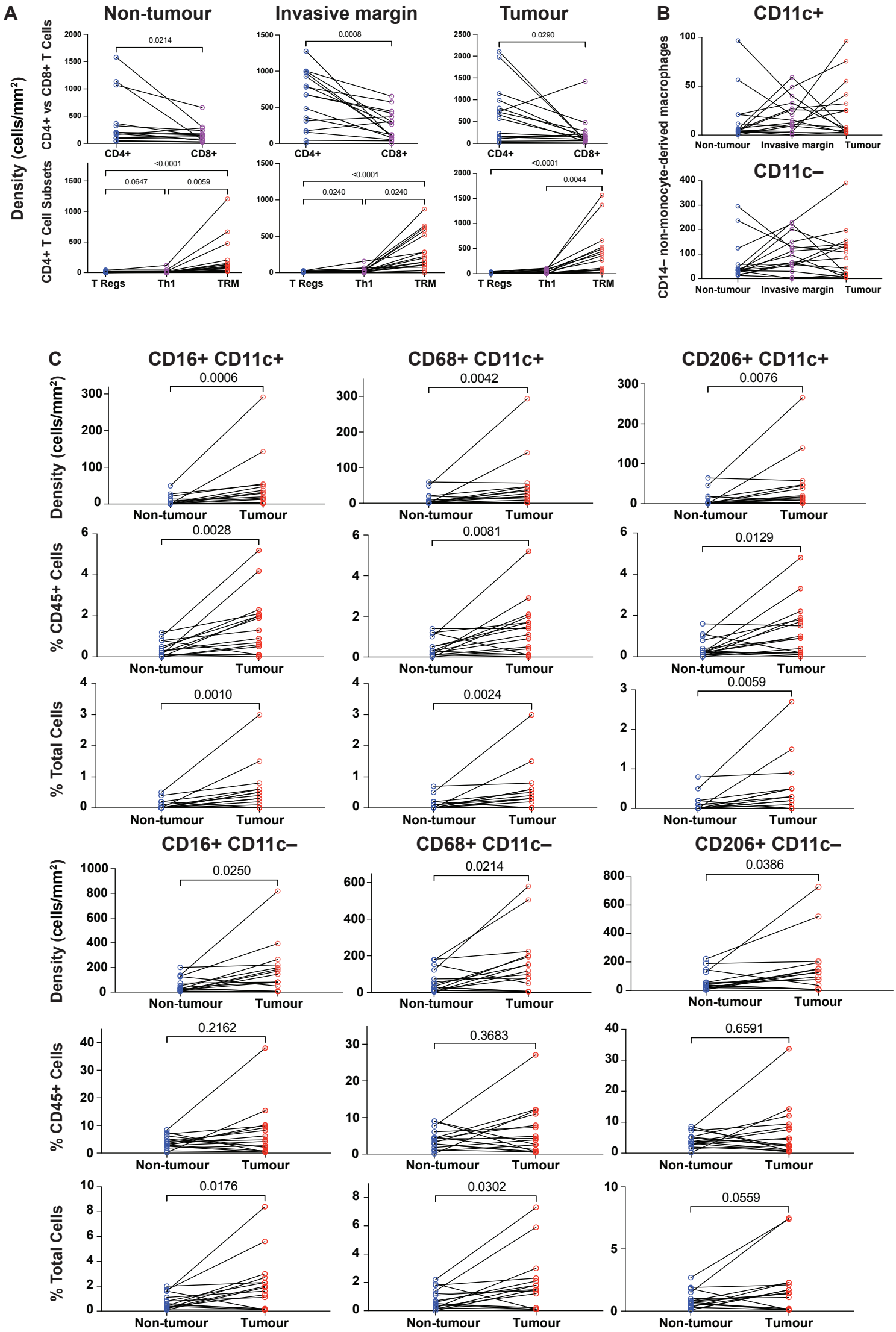
A
Non-tumour
Invasive margin
Tumour
Density (cells/mm²)
CD4+ vs CD8+ T Cells
CD4+ T Cell Subsets
0.0214
0.0008
0.0290
<0.0001
0.0647
0.0059
0.0240
0.0240
0.0044
CD4+
CD8+
T Regs
Th1
TRM
B
CD11c+
CD11c–
CD14– non-monocyte-derived macrophages
Non-tumour
Invasive margin
Tumour
C
CD16+ CD11c+
CD68+ CD11c+
CD206+ CD11c+
Density (cells/mm²)
% CD45+ Cells
% Total Cells
0.0006
0.0042
0.0076
0.0028
0.0081
0.0129
0.0010
0.0024
0.0059
CD16+ CD11c–
CD68+ CD11c–
CD206+ CD11c–
0.0250
0.0214
0.0386
0.2162
0.3683
0.6591
0.0176
0.0302
0.0559
Non-tumour
Tumour

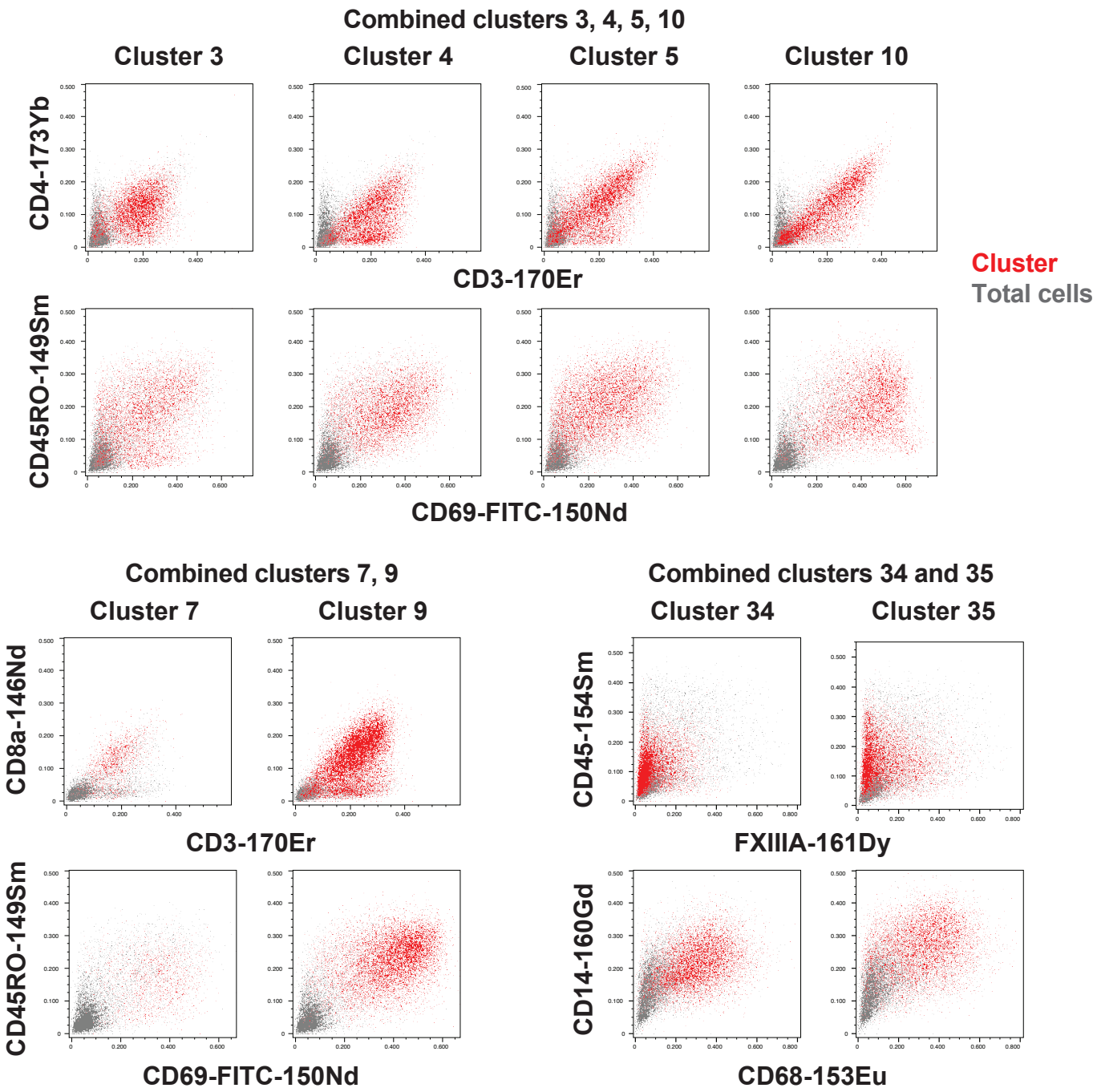
Combined clusters 3, 4, 5, 10
Cluster 3
Cluster 4
Cluster 5
Cluster 10
CD4-173Yb
CD3-170Er
CD45RO-149Sm
CD69-FITC-150Nd
Cluster
Total cells
Combined clusters 7, 9
Cluster 7
Cluster 9
CD8a-146Nd
CD3-170Er
CD45RO-149Sm
CD69-FITC-150Nd
Combined clusters 34 and 35
Cluster 34
Cluster 35
CD45-154Sm
FXIIIA-161Dy
CD14-160Gd
CD68-153Eu

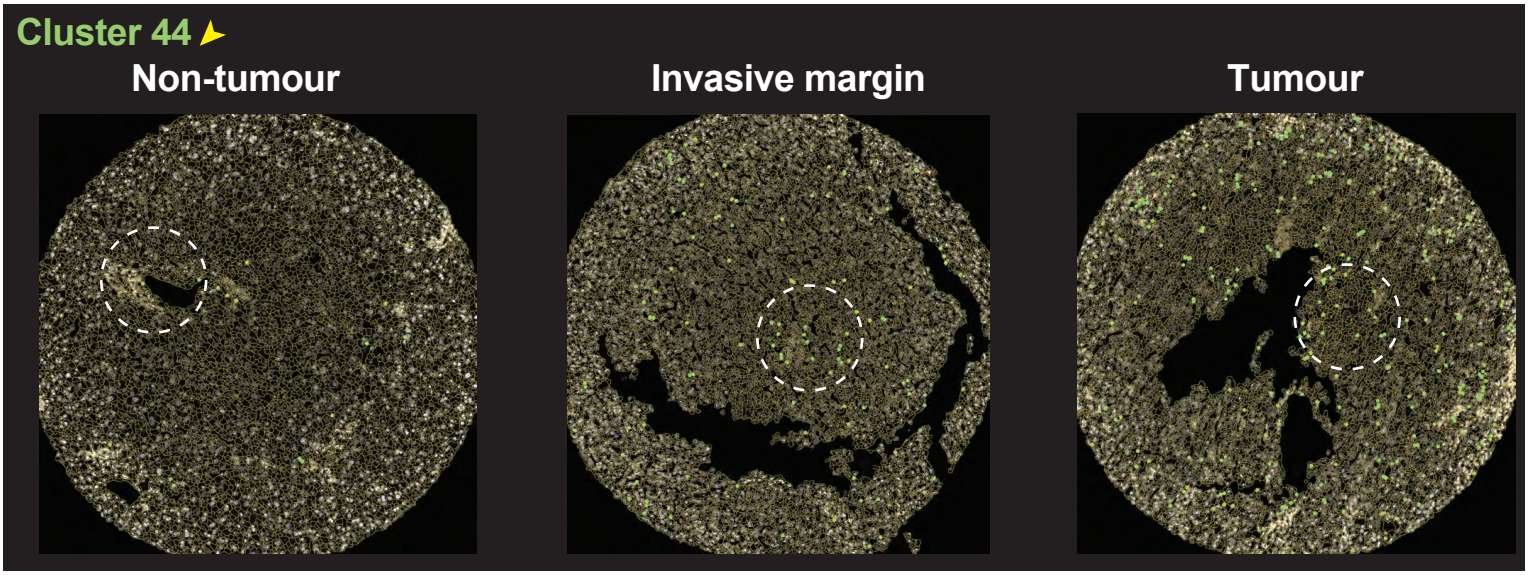

Cluster 44-44 interactions

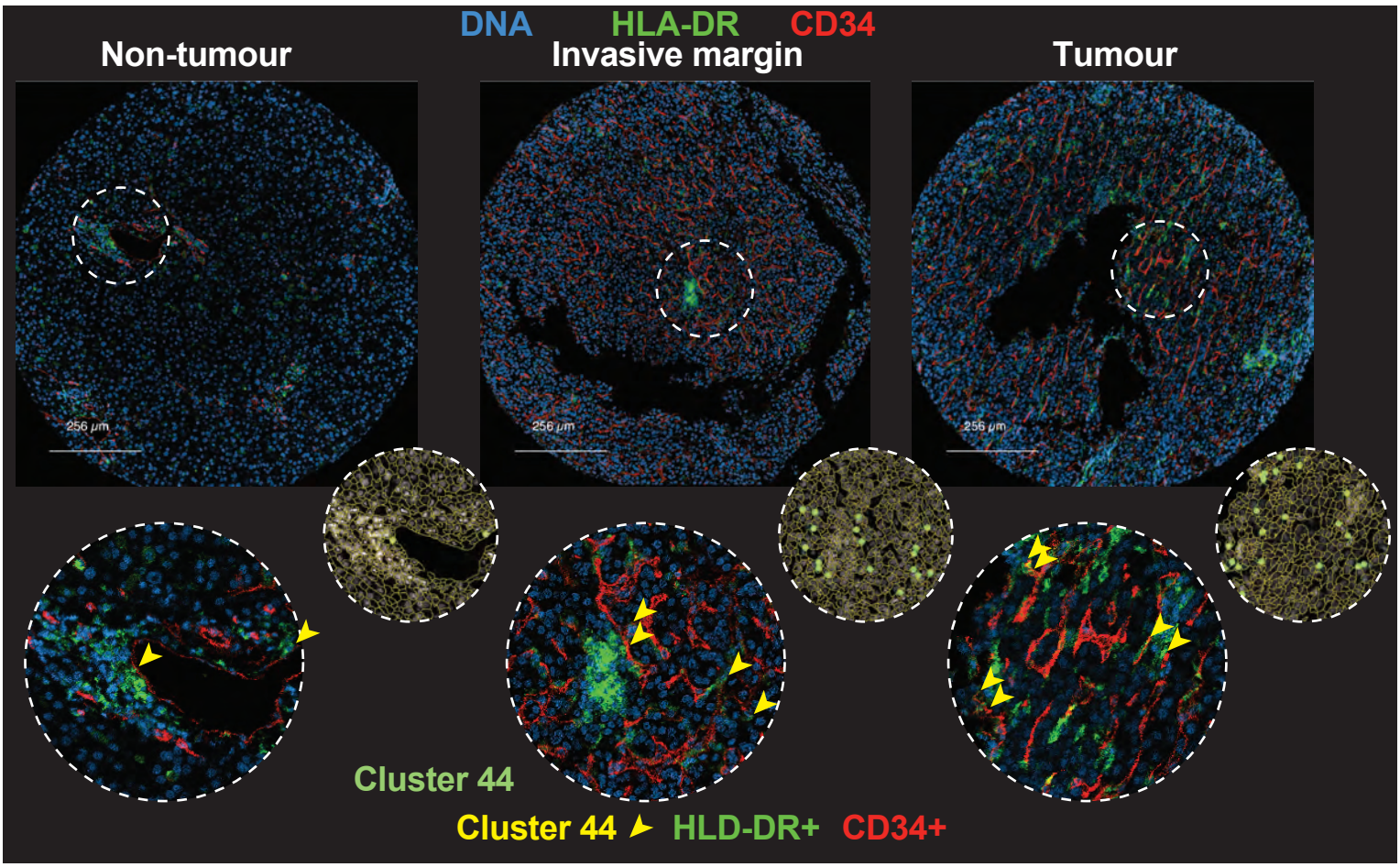

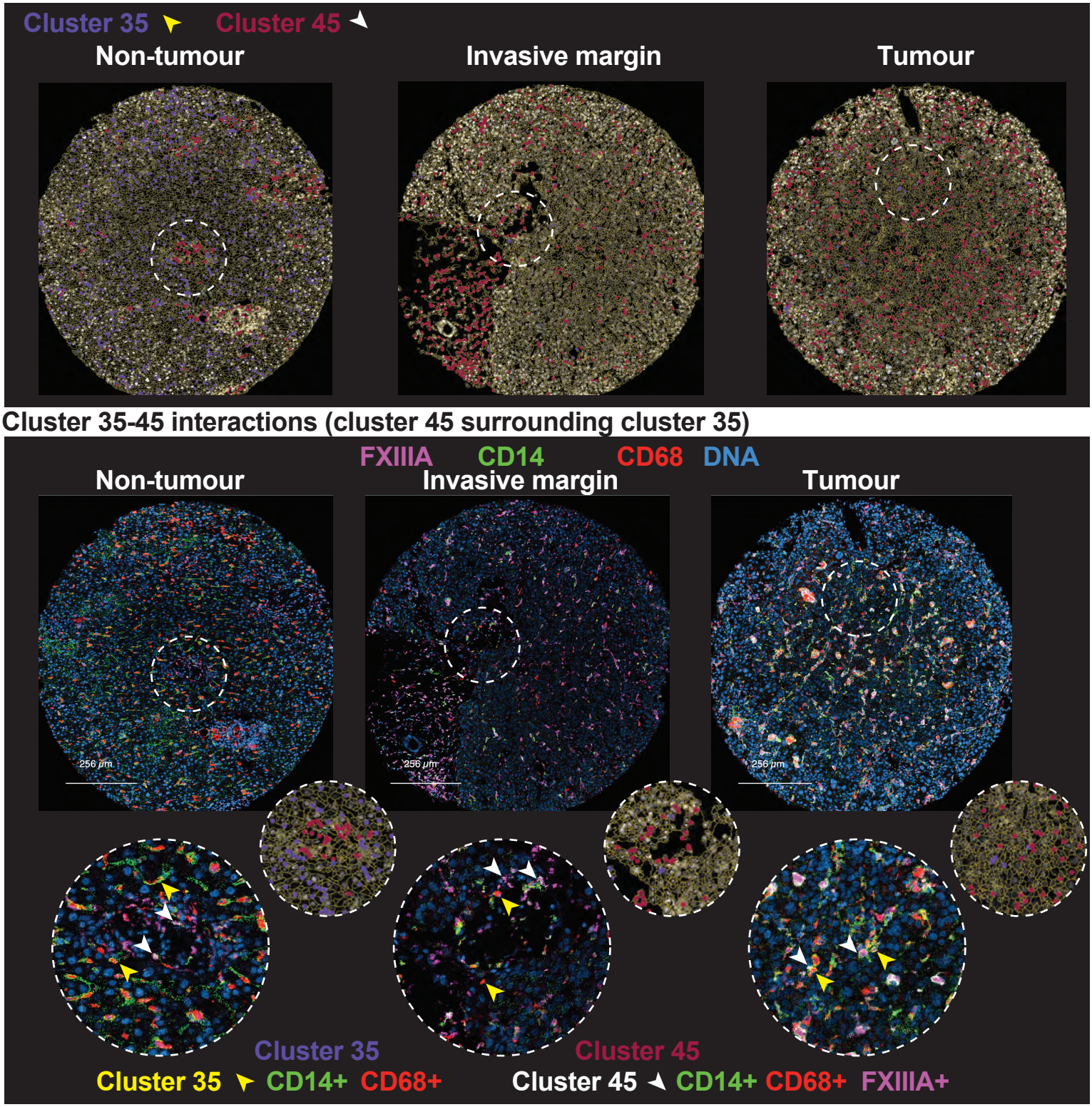
Cluster 35
Cluster 45
Non-tumour
Invasive margin
Tumour
Cluster 35-45 interactions (cluster 45 surrounding cluster 35)
FXIIIA
CD14
CD68
DNA
Non-tumour
Invasive margin
Tumour
256 µm
256 µm
256 µm
Cluster 35
Cluster 45
Cluster 35
CD14+
CD68+
Cluster 45
CD14+
CD68+
FXIIIA+

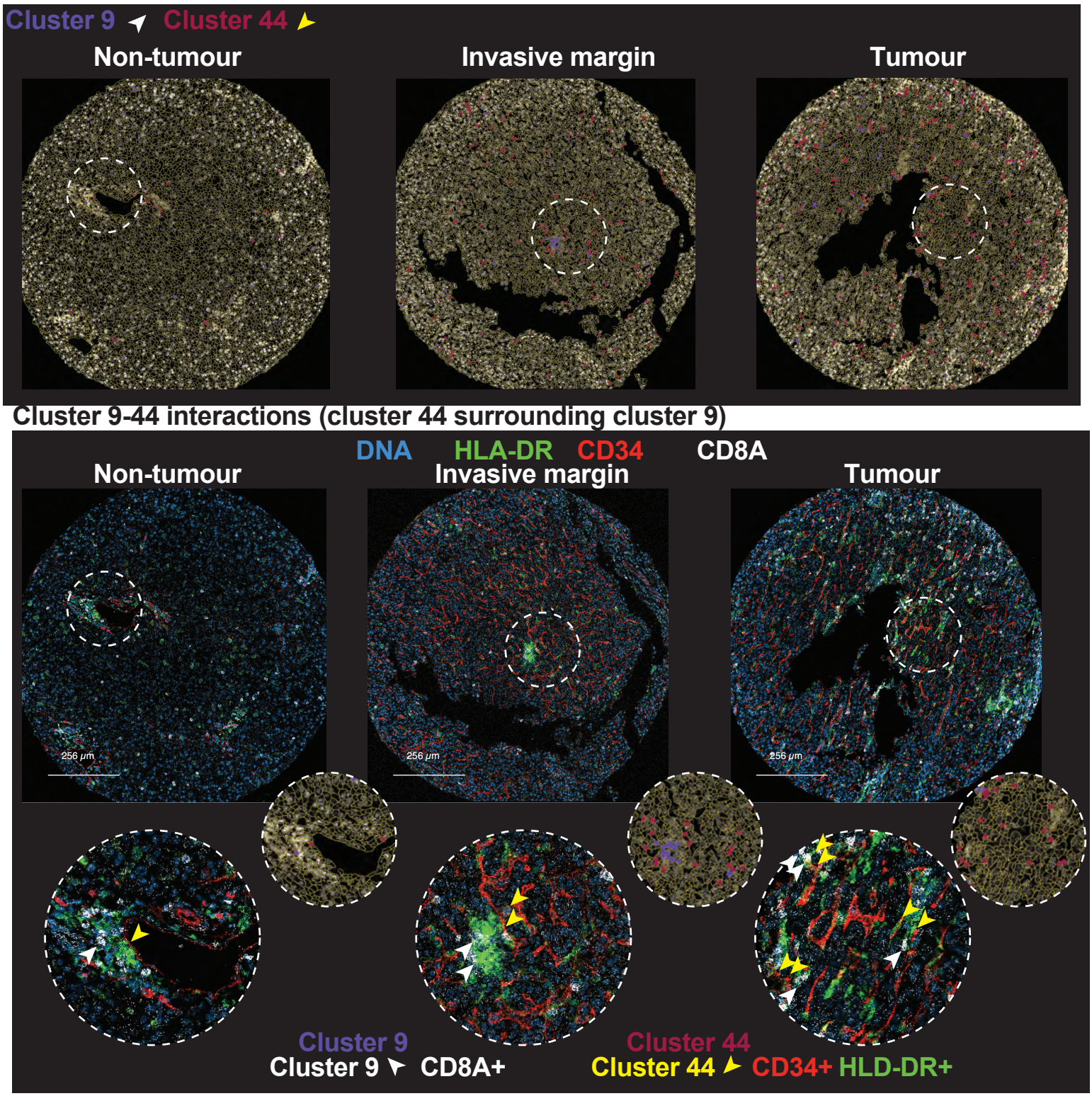
Cluster 9
Cluster 44
Non-tumour
Invasive margin
Tumour
Cluster 9-44 interactions (cluster 44 surrounding cluster 9)
DNA
HLA-DR
CD34
CD8A
Non-tumour
Invasive margin
Tumour
256 μm
256 μm
256 μm
Cluster 9
Cluster 9
CD8A+
Cluster 44
Cluster 44
CD34+
HLD-DR+

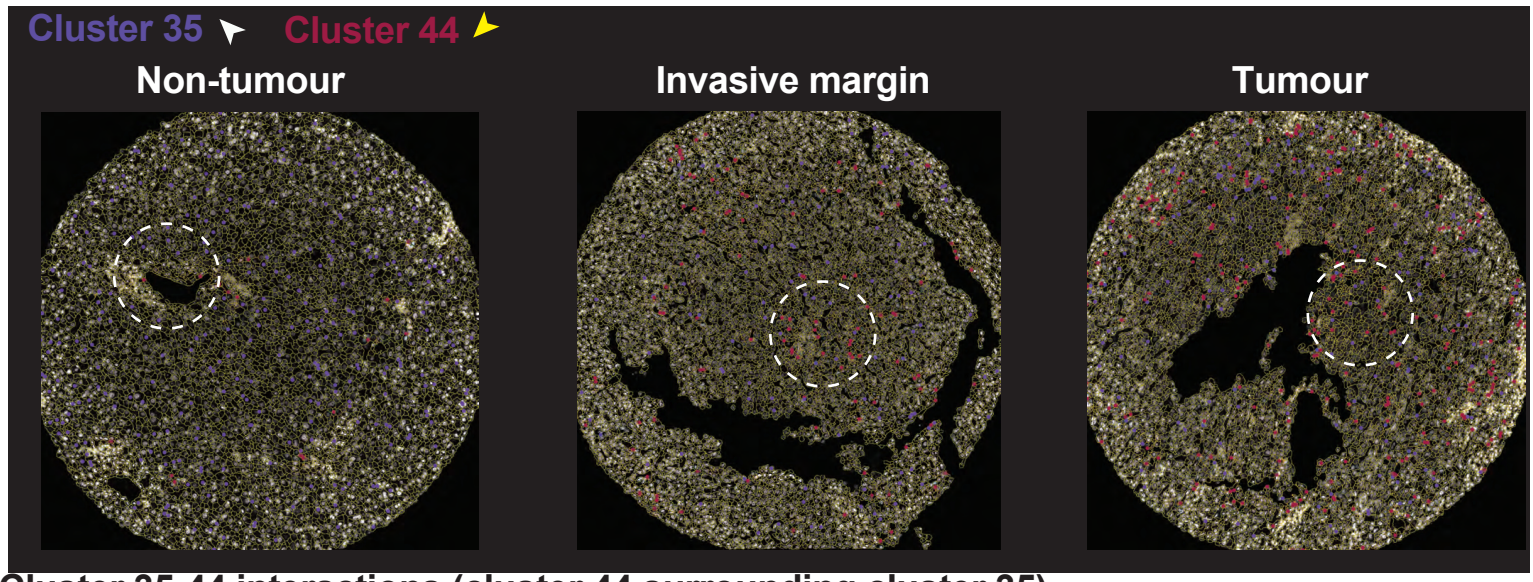

Cluster 35-44 interactions (cluster 44 surrounding cluster 35)

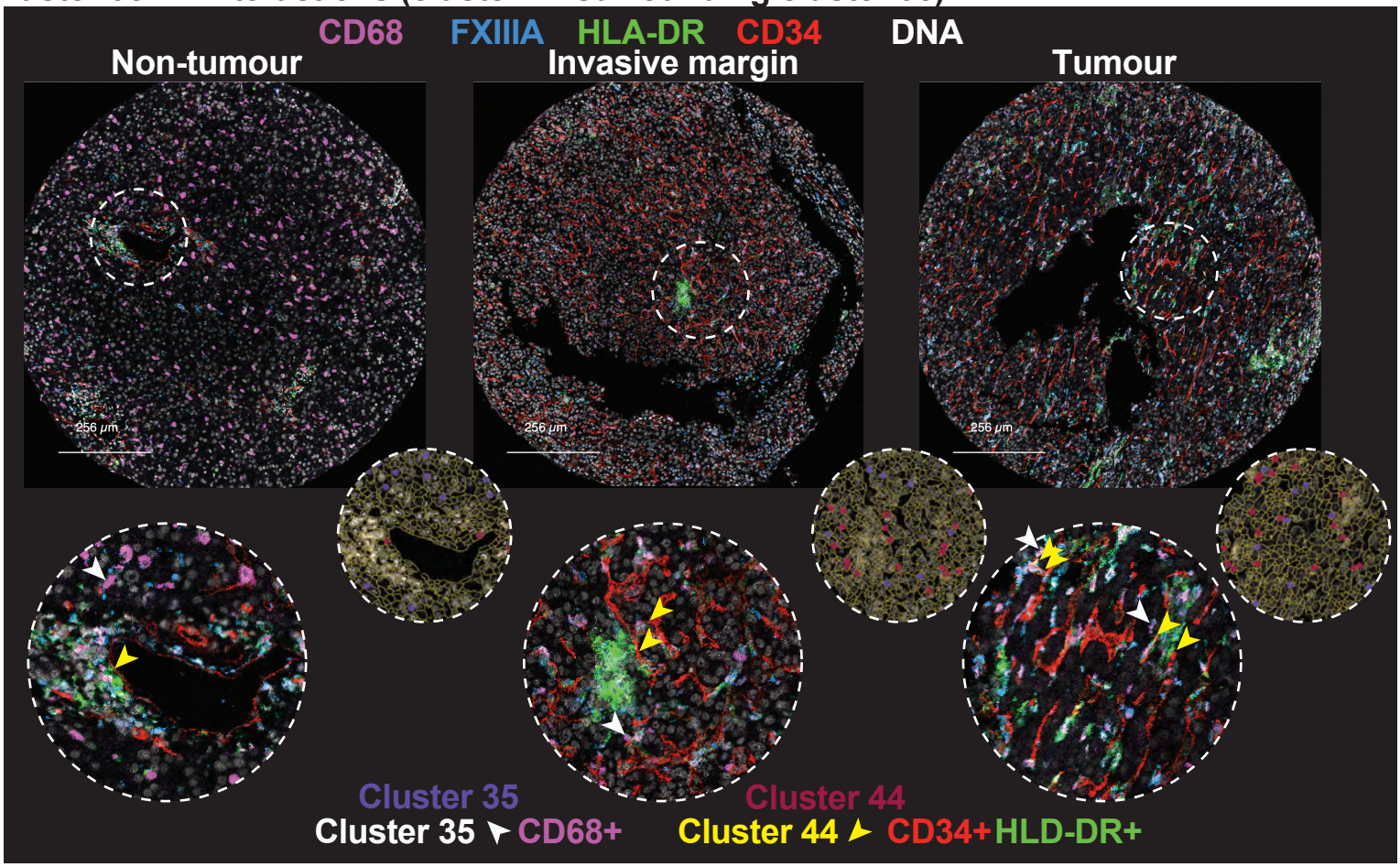

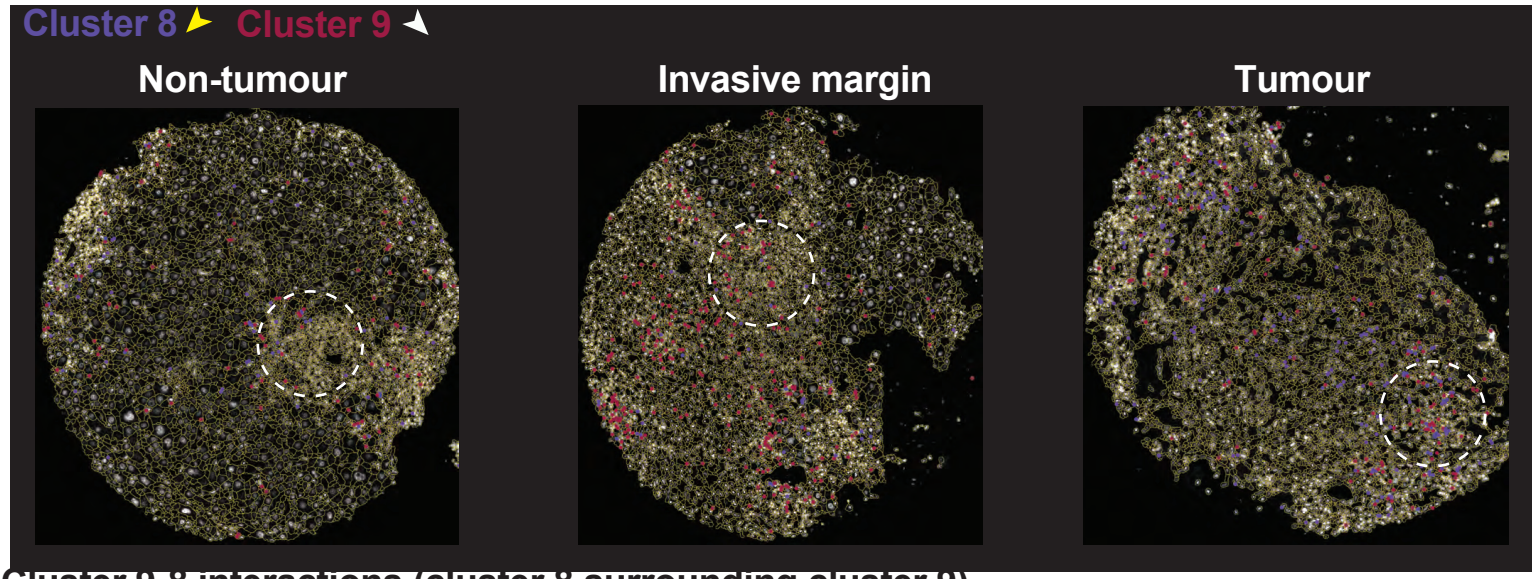

Cluster 9-8 interactions (cluster 8 surrounding cluster 9)

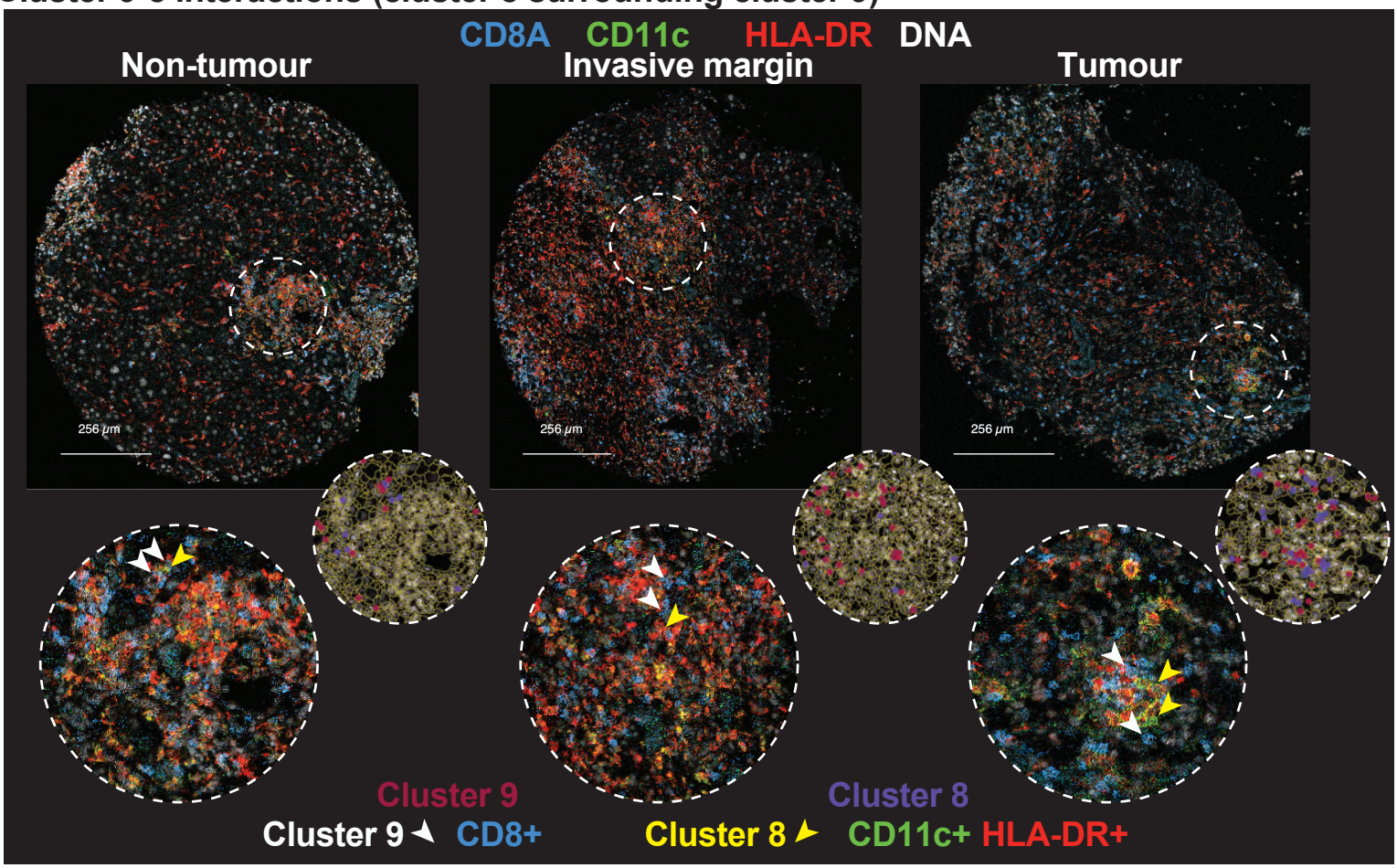

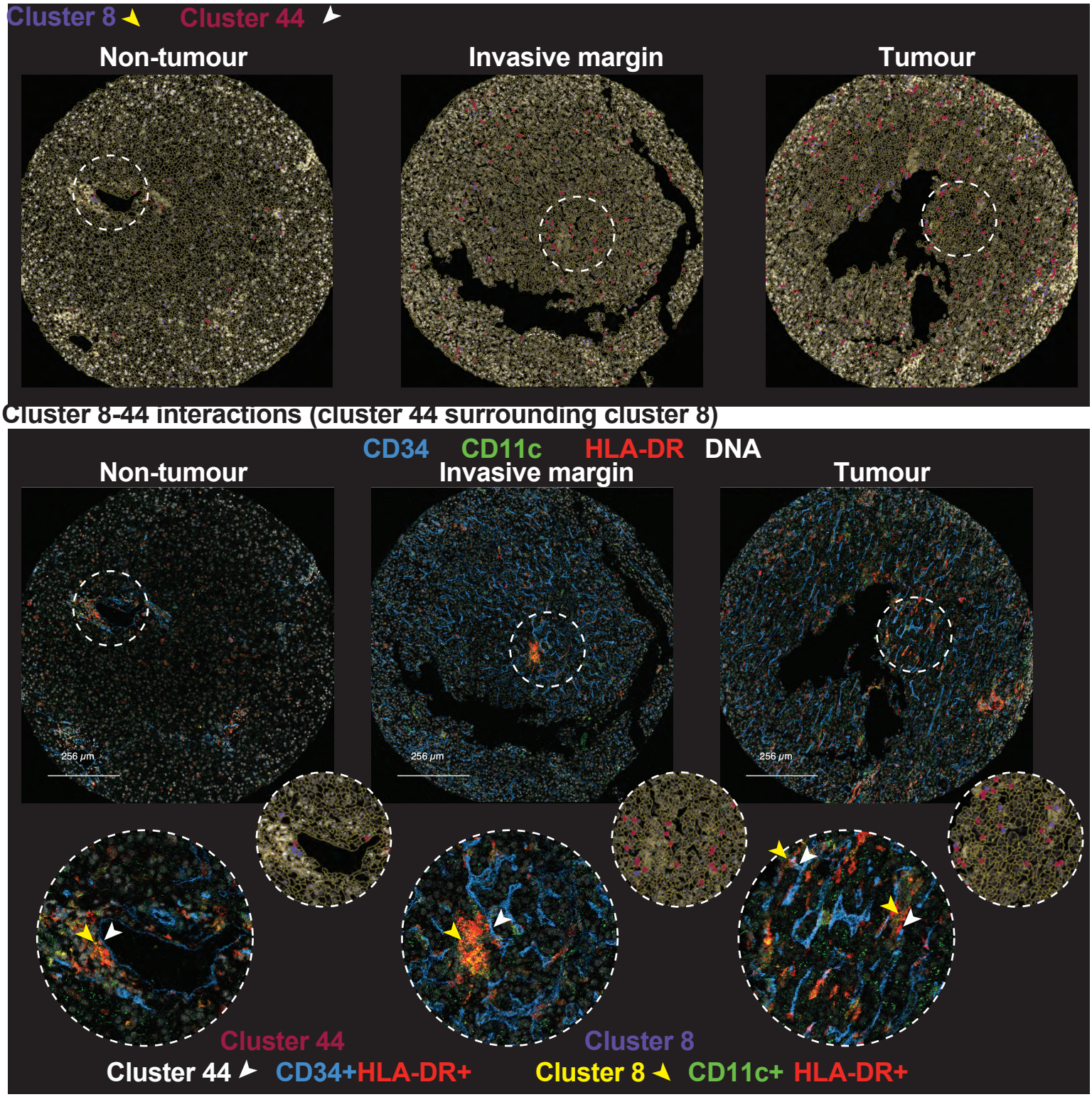
Cluster 8
Cluster 44
Non-tumour
Invasive margin
Tumour
Cluster 8-44 interactions (cluster 44 surrounding cluster 8)
CD34
CD11c
HLA-DR
DNA
Non-tumour
Invasive margin
Tumour
256 µm
256 µm
256 µm
Cluster 44
Cluster 8
Cluster 44
CD34+HLA-DR+
Cluster 8
CD11c+
HLA-DR+

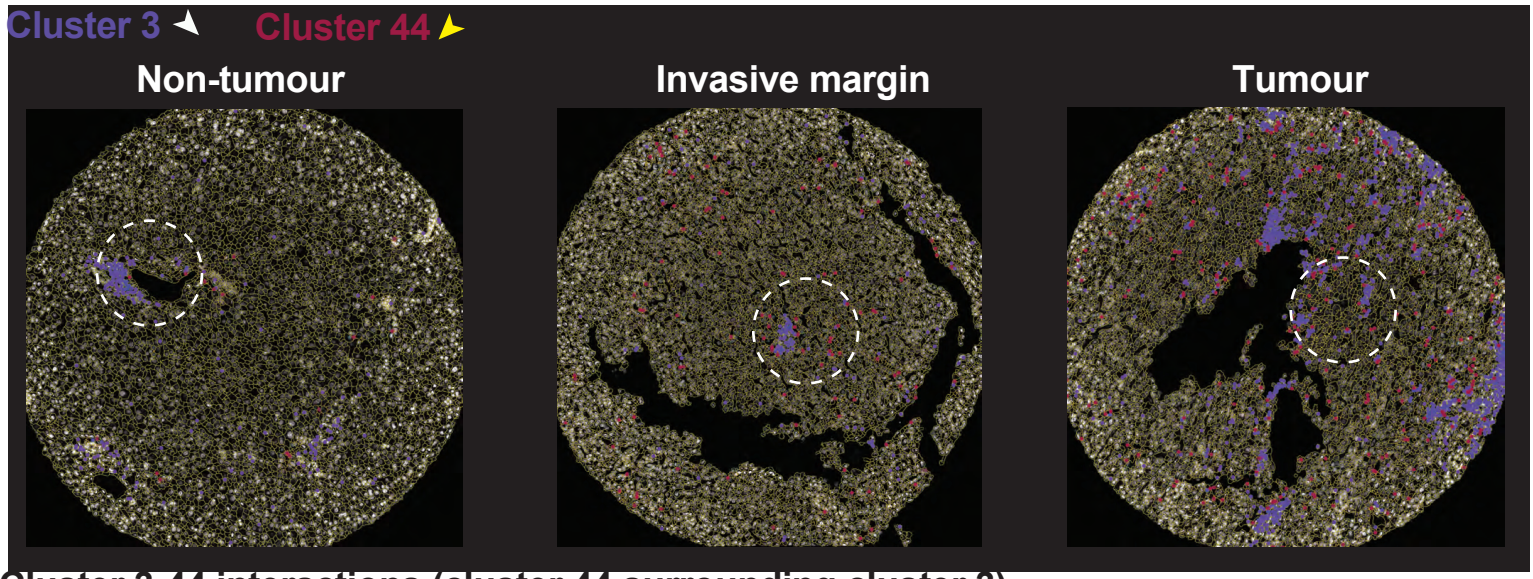

Cluster 3-44 interactions (cluster 44 surrounding cluster 3)

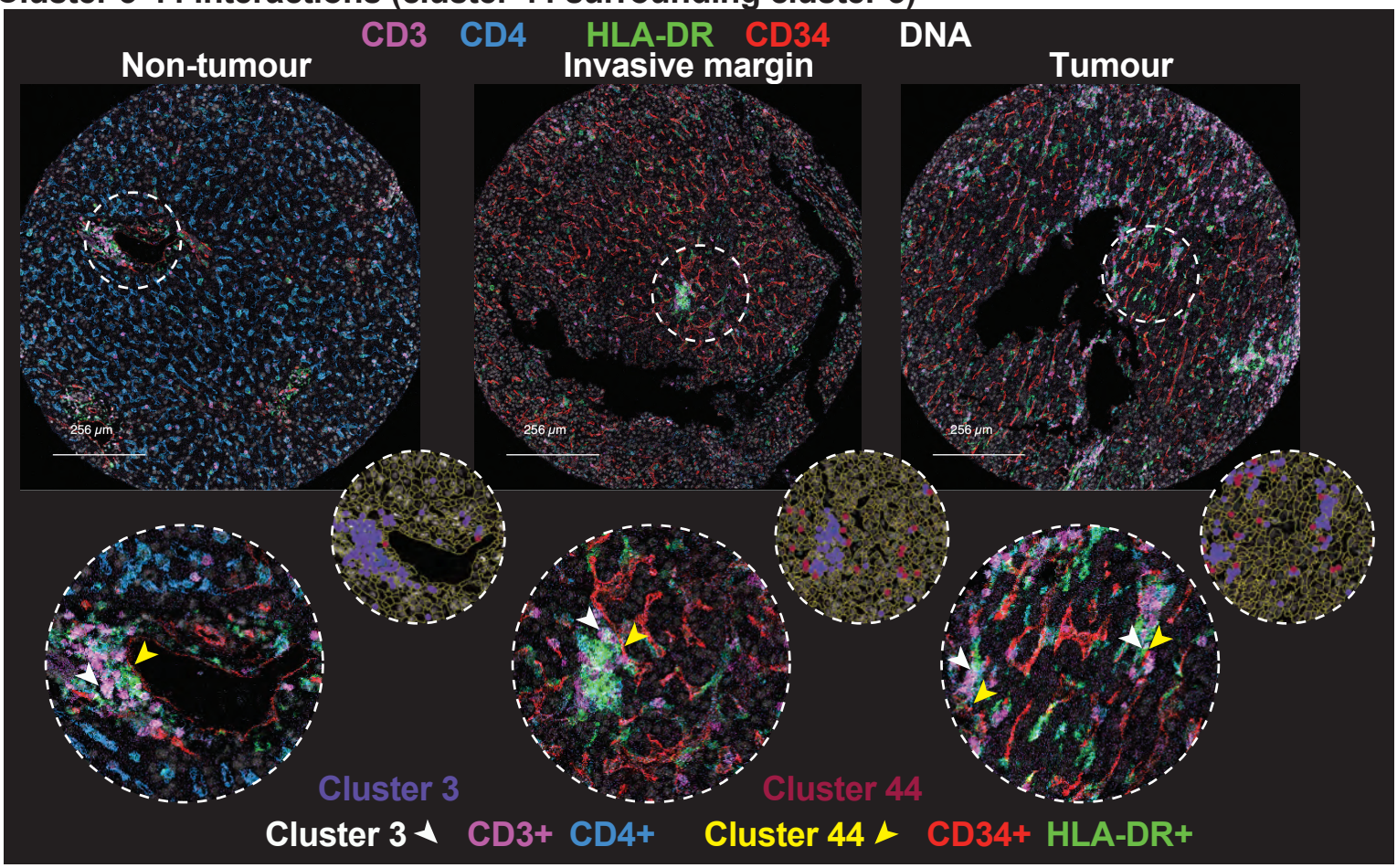

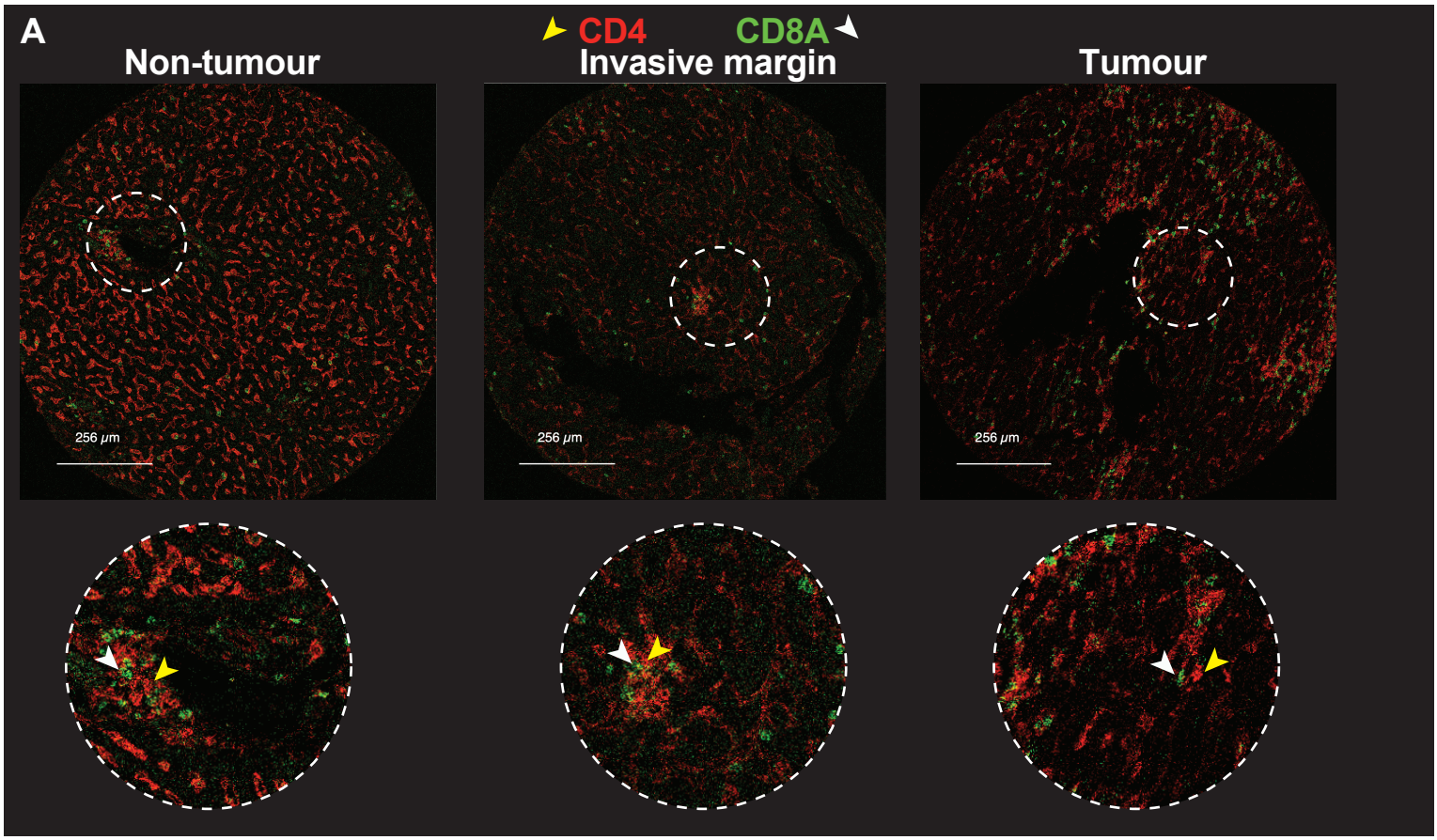

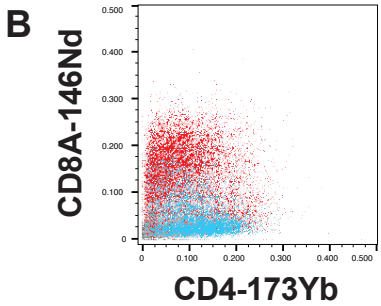

Cluster 3 (CD4+ T cells) Cluster 9 (CD8+ T cells) Total cells

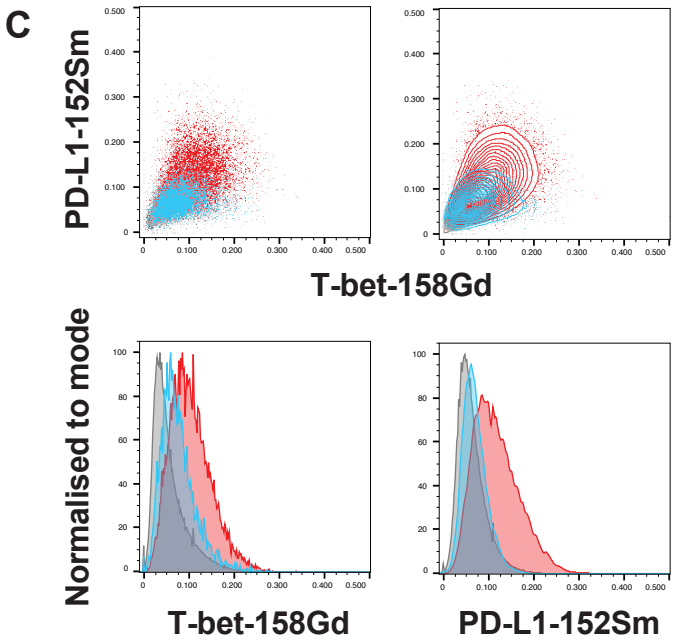

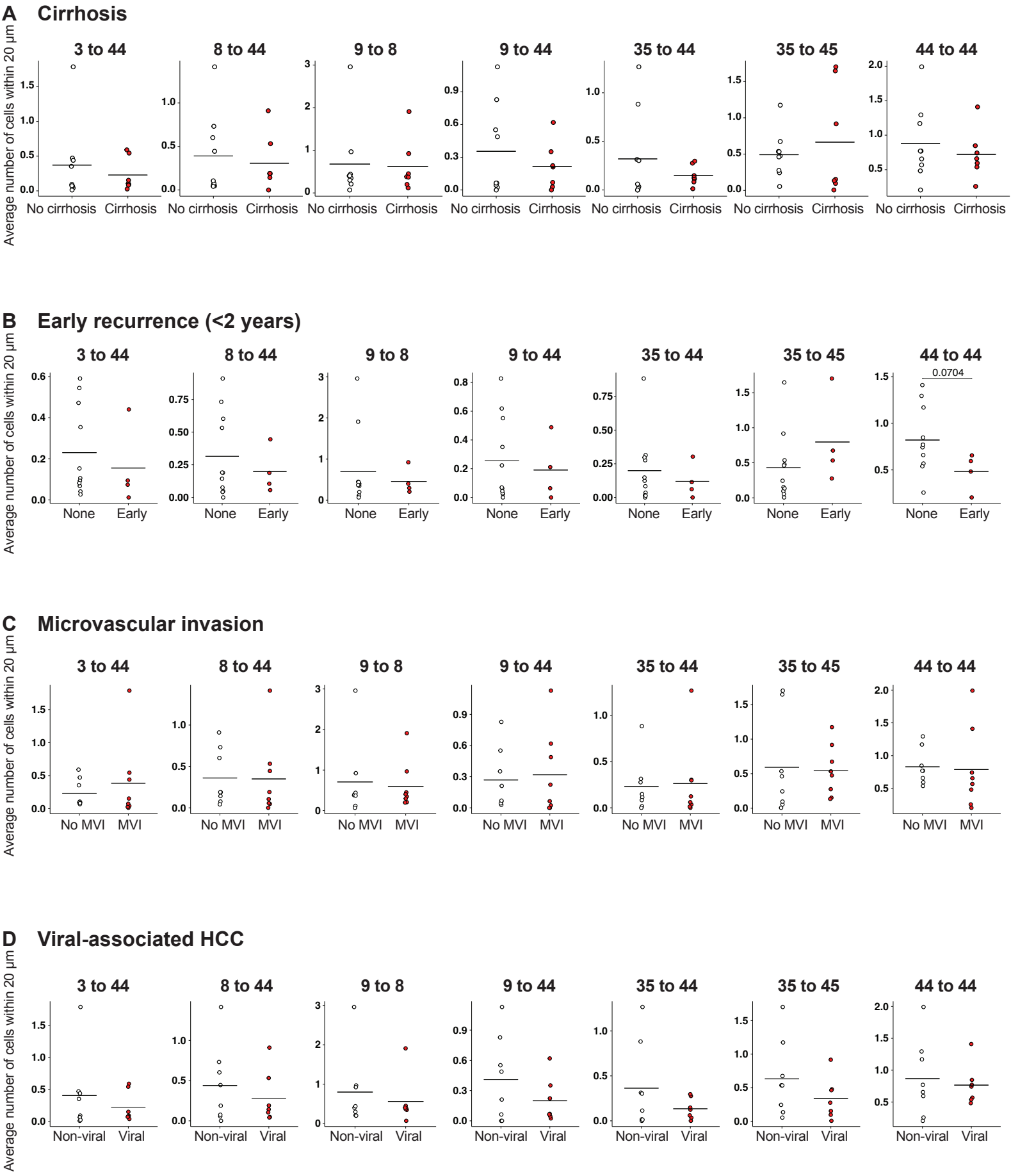
A
Cirrhosis
B
Early recurrence (<2 years)
C
Microvascular invasion
D
Viral-associated HCC
Average number of cells within 20 µm
3 to 44
8 to 44
9 to 8
9 to 44
35 to 44
35 to 45
44 to 44
No cirrhosis
Cirrhosis
None
Early
No MVI
MVI
Non-viral
Viral
0.0704

Supplementary Table 1: Imaging mass cytometry antibody panel

Metal	Marker	Clone	Species isotype	Company
89Y	a-SMA	1A4	Mouse IgG2a	R&D Systems
113In	Vimentin	D21H3	Rabbit IgG	CST
139La	CD57	HNK-1	Mouse IgM	BD Biosciences
141Pr	CD20	H1	Mouse IgG2a	BD Biosciences
142Nd	CD11c	EP1347Y	Rabbit IgG	Abcam
143Nd	Foxp3-biotin	236A/E7	Mouse IgG1	eBioscience
	Anti-biotin	1D4-C5	Mouse IgG2a	DVS
144Nd	MPO	E1E7l	Rabbit IgG	CST
145Nd	E-cadherin	36/E-cadherin	Mouse IgG2a	BD Biosciences
146Nd	CD8a	D8A8Y	Rabbit IgG	CST
147Sm	Podoplanin	polyclonal (cat #AF3670, batch #XXO0219081)	Sheep IgG	R&D Systems
148Nd	CD16	EPR16784	Rabbit IgG	Abcam
149Sm	CD45RO	UCHL1	Mouse IgG2a	BioLegend
150Nd	CD69	EPR21814	Rabbit IgG	Abcam
	Anti-FITC	FIT-22	Mouse IgG1	BioLegend
151Eu	HepPar1*	OCH1E5	Mouse IgG1	Santa Cruz
152Sm	PD-L1	E1L3N	Rabbit IgG	CST
	Cy3-donkey anti-rabbit	polyclonal (code 711-166-152, lot 122096)	Donkey IgG	Jackson ImmunResearch Laboratories
	Anti-Cy3	A-6	Mouse IgG1	Santa Cruz
153Eu	CD68	KP1	Mouse IgG1	BioLegend
154Sm	CD45	D9M8I	Rabbit IgG	Cell Signalling
155Gd	CD34*	QBend10	Mouse IgG1	Novus Biologicals
156Gd	CD86	polyclonal (cat #AF141NA)	Goat IgG	R&D Systems

158Gd	T-bet	D6N8B	Rabbit IgG	CST
159Tb	PD-L2*	D7U8C	Rabbit IgG	CST
160Gd	CD14	EPR3653	Rabbit IgG	Abcam
161Dy	FXIIIa	polyclonal (cat #SAF13A-AP, batch #AP1625-AR1)	Sheep IgG	Affinity Biologicals
162Dy	IgA*	3A5A5	Mouse IgG1	Proteintech
163Dy	CD11b	EPR1344	Rabbit IgG	Abcam
164Dy	SirPa	D6I3M	Rabbit IgG	Cell Signalling
165Ho	NaKATPase	EP1845Y	Rabbit IgG	Abcam
166Er	CD127	EPR2955(2)	Rabbit IgG	Abcam
167Er	CD66a	YTH71.3	Rat IgG2a	Abcam
168Er	Ki67	B56	Mouse IgG1	BD Biosciences
169Tm	CK8/18	5D3	Mouse IgG1	Leica
	AF647-donkey anti-mouse	polyclonal (code 715-606-150, lot 121469)	Donkey $F(ab')_2$ fragment	Jackson ImmunResearch Laboratories
	Anti-AF647/Cy5	CY5-15	Mouse IgG1	Sigma
170Er	CD3	polyclonal (cat #A045229-2)	Rabbit	Dako
171Yb	granzyme B	EPR8260	Rabbit IgG	Abcam
172Yb	CD206	685645	Mouse IgG2b	R&D Systems
173Yb	CD4	EPR6855	Rabbit IgG	Abcam
174Yb	HLA-DR	EPR3692	Rabbit IgG	Abcam
175Lu	CD303/BDCA2	polyclonal (cat #55427-1-AP)	Goat IgG	R&D Systems
176Yb	CD56	EPR2566	Rabbit IgG	Abcam
209Bi	DC-SIGN	polyclonal (cat # ab5715)	Rabbit IgG	Abcam

*Antibodies conjugated and titrated by our group. All others were conjugated by Sydney Cytometry or bought directly conjugated from Standard BioTools.